A CFD Investigation of the Two Phase Flow Regimes Inside the Bearing Chamber and De-aerator of a Jet Engine

Ryan Hehir

Thesis submitted to the faculty of the Virginia Polytechnic Institute and State University in partial fulfillment of the requirements for the degree of

Masters of Science
In
Mechanical Engineering

Srinath V. Ekkad
Hervé P. Morvan
Brain L. Vick

September 23rd 2016
Blacksburg, Virginia

Keywords: Jet Engines, Turbine Lubrication, Oil and Air Separation

A CFD Investigation of the Two Phase Flow Regimes Inside the Bearing Chamber and De-aerator of a Jet Engine

Ryan Hehir

Abstract

In a jet engine air and oil are mixed during removal from the bearing chamber. Before the oil can be recycled back into the system it must be separated from the air. This is accomplished through use of a de-aerator and breather. The oil air mixture enters the de-aerator first. The de-aerator is a vertical cylinder in which the air and oil enter from the top of the system. Gravity then pulls the oil down as it circulates along the outer wall of the de-aerator. The air is forced out through a top hole and sent to the breather where any oil droplets which remain are furthered separated. A pedestal is located near the bottom of the de-aerator. The pedestal creates a gap between itself and the de-aerator wall. Ideally this gap should be large enough to allow oil to flow through the gap without pooling on the pedestal, but small enough so that air does not flow through the gap. The oil will pool up on the pedestal and reduce the efficiency of the system. In this research, a 30° conical pedestal with a gap of 10.7% was tested. The results showed that the pedestal gap of 10.7% is too large and allows air to flow through the gap. The maximum water was 8.5% and the average water thickness was 5.11%. After studying both the previous experimental data and current CFD data, it is recommended further testing be conducted on pedestal gaps between 8.5% and 9.5%.

A CFD Investigation of the Two Phase Flow Regimes Inside the Bearing Chamber and De-aerator of a Jet Engine

Ryan Hehir

General Audience Abstract

In jet engines, the turbine provides power and thrust to the aircraft by spinning at high speeds. This spin is created through the expansions of the hot gases leaving the combustion chamber. To prevent the degradation of turbine it spins on lubricated ball bearings. However, the oil which lubricates these ball bearings increases in temperature due to its proximity to the turbine. To prevent the oil from deteriorating it must be recycled from the ball bearings allowing the oil to cool. In process of recycling the oil, air is also pulled out of the system. Before the oil can be reinserted to the ball bearings it must first be separated from the air. This is accomplished in the de-aerator. In the de-aerator the oil and air mixture enter the side of a long cylinder. The oil flows down the side of this cylinder and out vents at the base. The air flows out vents at the top of the cylinder. Towards the base of the de-aerator is a pedestal, which creates a gap between itself and the wall. This gap should create a seal between the oil and the air, so that air does not flow through the gap and oil does not pool on top of the pedestal. Using CFD (Computational Fluid Dynamics), a software which simulates fluid flow, it was determined that pedestal gap should be between 8.5% and 9.5% of the radius of the de-aerator.

Table of Contents

List of Figures

List of Tables

Nomenclature

Symbol	Description
av	Air Vent
B	Damping Factor
d	Diameter
D1	Y Junction Pipe Diameter
D2	De-aerator Diameter
eff	Effective
f	Additional Forces
g	Gravity
G	Gas
h	Film thickness
inl	Inlet
l	Unit Vector
i, j, k	Cartesian Indices
k	Turbulent Kinetic Energy
kPa	Kilopascal
lv	Liquid Vent
L	Liquid
m	Mass
$\dot{m}$	Mass Flux
Ma	Mach Number
max	Maximum
min	Minimum
min.	Minute
P	Pressure
p	Particle
Pa	Pascal
R	Bearing Chamber Radius

Re	Reynolds Number
s	Second
sc	Scavenge
t	Time
turb	Turbulence
u, v, w	Velocity Components
$\dot{V}$	Volumetric Flowrate
vt	Vent
x, y, z	Cartesian Coordinates
$\Delta x, \Delta y, \Delta z$	Cell Gradients
'	Fluctuation Indices
~	Normalized Indices
*****	Dimensionless Variable
$\rightarrow$	Vector

Greek Symbol	Description
α	Volume Fraction
Δ	Difference
ρ	Density
σ	Surface Tension
τ	Shear Stress
ϑ	Angle
ε	Turbulence Dissipation Rate
μ	Dynamic Viscosity
ω	Frequency

Abbreviations	Description
2D	Two Dimensional
3D	Three Dimensional
CFD	Computational Fluid Dynamics
CFL	Courant-Lewy-Friedrich
CR	Cruise
DPM	Discrete Phase Model
GI	Ground Idle
HP	High Pressure
KIT	Karlsruhe Institute for Technology
MTO	Max Takeoff
RANS	Reynolds Averaged Navier Stokes
RR	Rolls Royce
SC	Scavenged
SR	Scavenge Ratio
SST	Shear Stress Transport
UTC	University Technology Center
VOF	Volume of Fluid

1.0 Introduction

Since their invention, jet engines have made great strides in improving power and efficiency. Demands for future jet engines continue to rely on increasing efficiency and reducing emissions. Previously to achieve improved efficiency, engine manufacturers have looked to increase the air pressure and temperature within the engine, as these factors have the largest impact on power and efficiency. However, recently jet engine efficiency has been slowed due to the turbine temperature reaching the melting point of the turbine blades [1]. This has led to an increased need to improve efficiency elsewhere in the engine including the air syphoning systems, oil systems, and overall engine design [2]. This research will use Computational Fluid Dynamics (CFD) to study ways to improve engine efficiency.

1.1 Oil Systems

Due to the high turbine speeds in jet engines, a need to improve the lubrication system within the jet engine has arisen. The job of the oil system is to prevent the degradation of the engine by decreasing the friction created from the spinning turbine, while also providing cooling to high temperature components. Additionally the oil system should remove any debris that has eroded off the turbine [2, 3]. These functions significantly increase the life of the engine and are essential to operating the engine [4].

Figure 1 shows the oil system within a Rolls Royce Trent 500 engine. This engine, along with most jet engines, is a self-contained circulatory engine. This means that oil is not wasted in the engine and is instead cycled through the engine and continually reused. Since the oil is used to lubricate the turbine shaft, the oil can reach high temperatures due to the heat of the turbine. By recirculating the oil throughout the lubrication system, the oil is allowed to cool [3]. This prevents degradation of the oil and keeps the system running optimally.

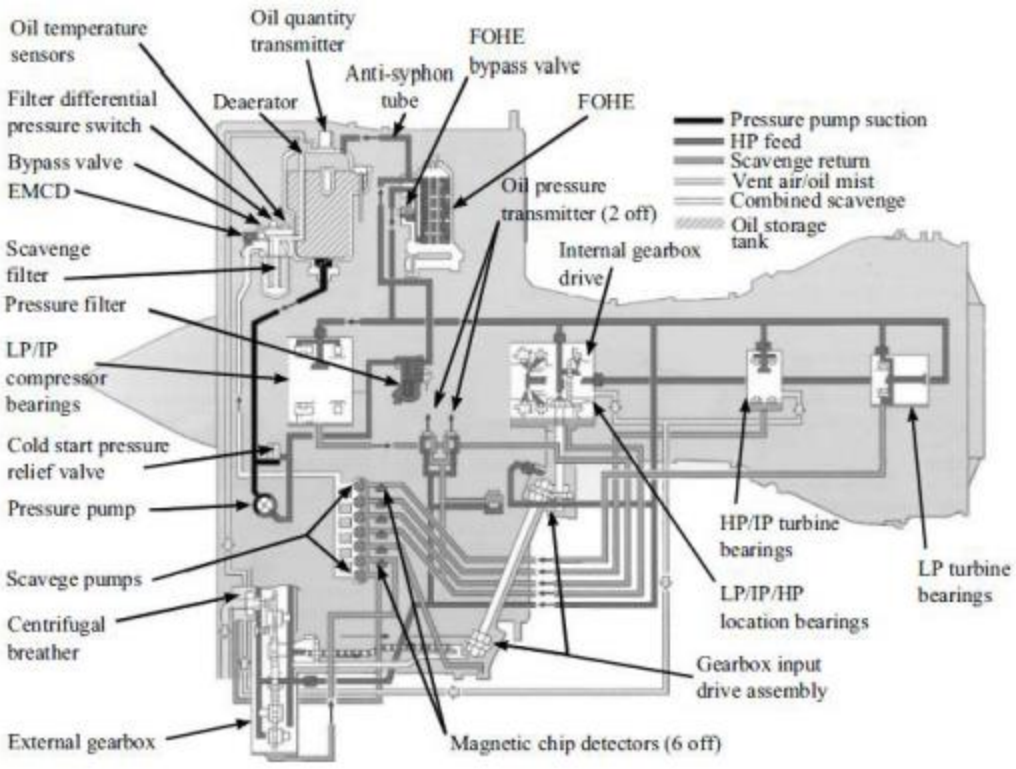

Figure 1: The oil system of a Trent 500 engine (Rolls Royce, 2005) [2]

.

The oil system of a jet engine can be divided into three sections: the feed system, the scavenge system and the vent system. The purpose of the feed system is to supply oil to parts of the engine where lubrication is needed [5]. These locations are primarily the bearing chambers and the gearboxes. Air is fed into the bearing chambers and gearboxes in order to provide a seal for the oil [2]. As the oil lubricates these components, it collects on the side walls of the bearing chambers and gearboxes.

The scavenge system then syphons the oil that collects on the side walls using oil sumps [2]. However, when the oil sumps remove the oil from the bearing chambers and gearboxes, they also remove air from the system. While a portion of the air is vented from the bearing chambers and gearboxes using an air vent, a significant amount of air is still syphoned with the oil. This creates complex two phase flow in the syphon tubes. The ratio of the volumetric flowrate of oil into the system and the volumetric flowrate of oil and air out of the system is known as the scavenge ratio (SR) and is shown in Equation 1.1 [2].

$$SR = \frac{\dot{V}_{total}}{\dot{V}_{liquid}} = \frac{\dot{V}_{sc}}{\dot{V}_{in,l}} = \frac{\dot{V}_{sc,g} + \dot{V}_{sc,l}}{\dot{V}_{sc,l} + \dot{V}_{vt,l}} \tag{1.1}$$

In Equation 1.1, $\dot{V}_{sc}$ is the volumetric flowrate of the scavenged oil and air. $\dot{V}_{in,l}$ is the volumetric flowrate of oil into the system. $\dot{V}_{sc,g}$ is the volumetric flowrate of air

syphoned from the system. $\dot{V}_{sc,l}$ is the volumetric flowrate of oil syphoned from the system. Lastly, $\dot{V}_{vt,l}$ is the volumetric flowrate of any oil that escapes through the air vents. Typically, double the volumetric flowrate of air is syphoned from the system compared to oil. This corresponds to a scavenge ratio of 3 [6].

In order to replenish the air within the bearing chambers and gearboxes, air is syphoned from the compressor. While the vast majority of the air that is syphoned from the compressor is used to cool the turbine blades, a small percentage is fed into the bearing chambers and gearboxes in order to maintain the sealing air within the system [2].

Once the oil and air mixture has been removed from the bearing chambers and gearboxes, the oil must be separated from the air. The separation of the oil and air first occurs in the de-aerator. After the mixture passes through the de-aerator, the oil and air are sent to the centrifugal breather for further separation. Once the oil is separated from the air, the oil is sent back into the bearing chambers and gearboxes to provide lubrication, while the air is vented from the system [5].

Separating the oil and air is necessary because by separating the oil and air, the amount of oil that is vented outside engine is minimalized. This not only reduces the loss of oil throughout engine operation, but also reduces the amount of greenhouse gas produced by the engine [7]. Additionally, air in the oil reduces the oils lubricating and cooling properties of the oil. This in turn creates a lower quality lubricant which reduces the life of the engine.

1.2 Bearing Chamber

The bearing chamber of a jet engine can be viewed in Figure 2 which shows a cylinder enclosing the the turbine shaft. The turbine shaft then sits on a set of lubricated ball bearings. These ball bearings allow the turbine to spin at high speeds while reducing friciton. As the turbine shaft spins on the ball bearings, oil is forced off of the ball bearings due to the angular velocity of the turbine shaft [2]. This causes the oil to collect on the sides of the bearing chamber. In Figure 2 the oil can be seen in gray [8].

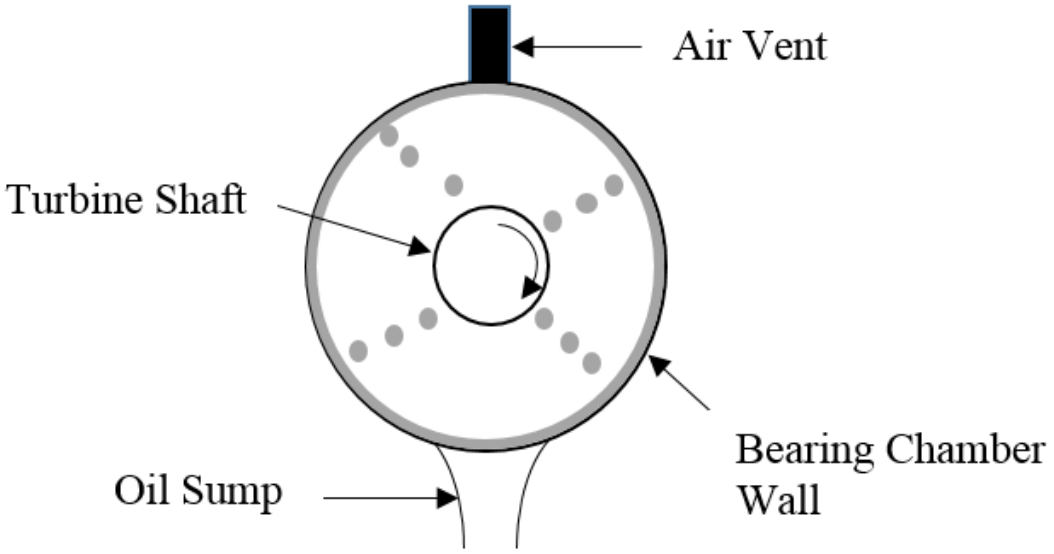

Figure 2: Basic design for a jet engine bearing chamber [8].

As previously stated, oil has to be removed from the system in order to cool the bearing chamber and prevent oil buildup. Due to the complex flow patterens within the bearing chamber, the oil and air form a intricate two phase mixture. Therefore, when oil is removed from the system using the oil sump, air is also removed [5]. Additionally, air and a small percentage of oil are vented out of the bearing chamber. The turbine shaft which drives the flow operates throughout a range of speeds depending on the flight condition. These speeds are ground idle (GI), max takeoff (MT), and cruise (CR). These mutliple turbine speeds can complicate the flow within the bearing chamber even further. Therefore, studies have been conducted on how reduce the scavenge ratio of the bearing chamber and increase effieciency of the oil and air separation.

1.2.1 Bearing Chamber Previous Research

Previous research on the two phase flow within the bearing chamber of a jet engine has been conducted primarily at the University Technology Centre (UTC) at the University of Nottingham and the Karlsruhe Institute for Technology (KIT). Experimental data on the oil film thickness has been studied by Gorse et al. [9] and Chandra and Simmons [10]. Both studied the oil flow within a bearing chamber with fluid injection from the turbine shaft. However, Gorse et al. used the KIT bearing chamber geometry which is used in this research and can be seen in Figure 3. Gorse et al. experimental results have been compared to CFD trial conducted by Adeniyi [5]. Adeniyi used Discrete Phase Model-Volume of Fluid (DPM-VOF) model to simulate the results. The volume of fluid model was validated for rotational flow in a chamber by Young and Chew.

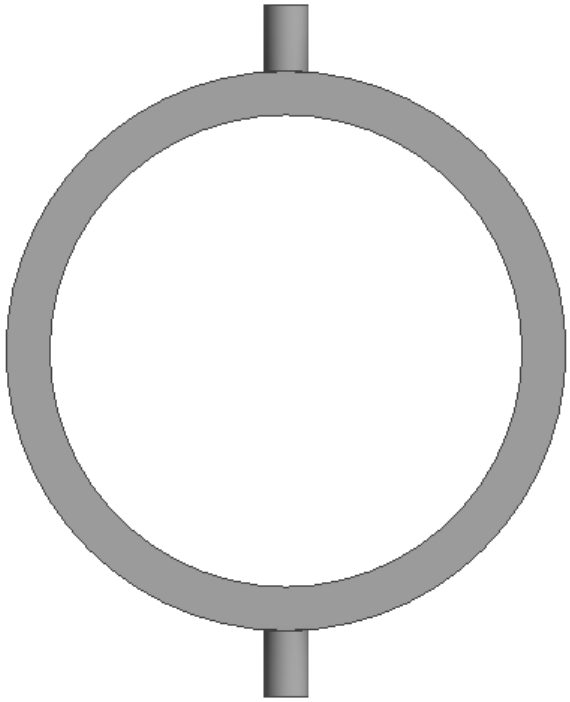

Figure 3: The KIT bearing chamber geometry used by Grose et al. and Adeniyi [5, 9].

Gorse et al. and Adeniyi conducted trials for numerous shafts speeds including 4000, 6000, 8000, 12000, and 16000 rpm [5, 9]. In these experiments, oil is injected as droplets from the turbine shaft. Additionally, there are vents at the top and bottom of the bearing chamber. These vents drain oil and air from the chamber.

In the experiments, the results for both experimental and CFD compare reasonably with only an 8.7% over prediction in the film thickness for the CFD [5, 9]. Their results primarily show the effect of the vents with the oil film thickness at zero at the vents and then slowly reaching a maximum film thickness slightly before the next vent. Additionally, the results show a decrease in film thickness at higher shaft speeds [5, 9]. Also, additionally, pooling can be seen in the lower left quadrant of the geometry due to the effects of gravity.

1.2.2 Bearing Chamber Objectives

The oil and air separation can be aided by increasing the percentage of oil removed from the oil and thus decreasing the scavenge ratio. Gorse et al. and Adeniyi's results are both dominated by the presence of the vents. These vents represent the sump in the actual bearing chamber. However, by removing the vents, natural buildup of the oil film can be studied. This can allow better placement of the sump in order to drain more oil from the

bearing chamber and increase efficeincy. Therefore, the objective of this research for the bearing chamber is as follows:

1. Investigate the effects of turbine shaft speeds at 500, 2000, 4000, and 8000 rpm on oil film thickness.
2. Investigate how the oil film thickness varies with respect to its angle from the center of the turbine shaft.

1.3 De-aerator

Once the oil and air mixture exits the bearing chamber, it is pumped to the de-aerator. Figure 4 shows the current de-aerator design. The purpose of the de-aerator is to separate the oil from the air. Figure 4 shows a cross sectional view of the de-aerator in which the oil flow can be seen in green and the air flow can be seen in orange. The oil and air both enter the de-aerator from an inlet pipe at the top of the cylinder. Then the oil circulates along the side of the vertical cylinder. As the oil circulates down the side of the de-aerator, it reaches the pedestal. There is a gap between the pedestal and the de-aerator wall. The gap allows only the oil to flow beneath the pedestal and then out the oil vent. The air circulates downward within the inner section of the de-aerator until it hits the pedestal. The pedestal reverses the axial velocity of the air and creates an air vortex moving up the de-aerator and out the air vent [11, 12]. Once the air comes out of the air vent, there is still small amount of oil mixed in the air. This air and oil mixture is then sent to the centrifugal breather where the oil and air are separated further [13].

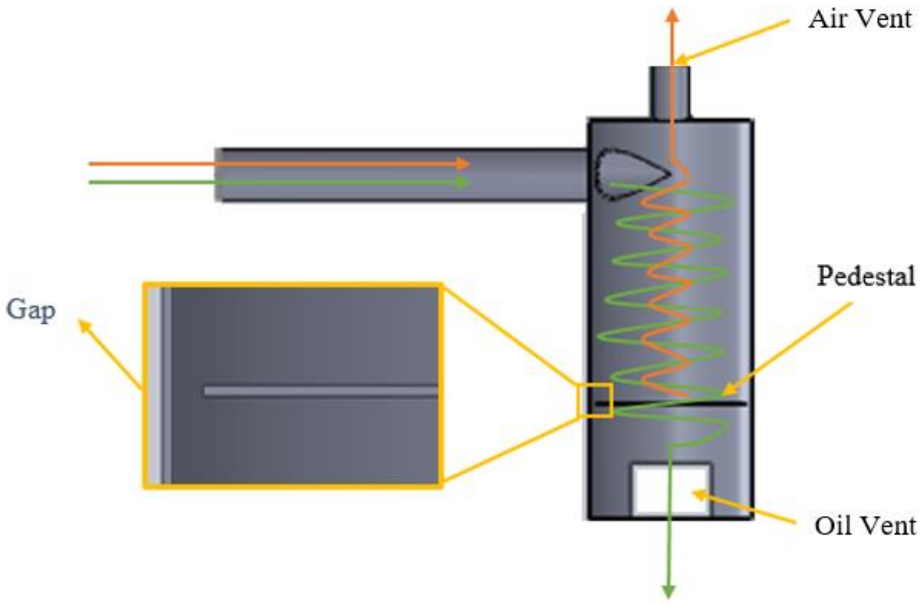

Figure 4: The two phase flow separation of oil and air in the de-aerator.

This de-aerator design is currently in use in the Rolls Royce Trent 1000 engine. Presently, the pedestal gap is smaller than the oil film thickness. This causes the oil to pool on top of the pedestal. As the oil pools on top of the pedestal, it is subject to the shear force from the air reversing direction. The air is then able to pick up droplets of oil and carry those droplets out of the air vent. Therefore, the pedestal gap needs to be the same as the oil film thickness [6]. However, if the pedestal gap is too large, it allows air to flow through the gap and out the oil vent. This then puts air into the oil tank and reduces the quality of the oil. This problem with the de-aerator is most prominent when the engine is in ground idle.

1.3.1 De-aerator Previous Research

Previous research for the de-aerator has been conducted experimentally by Brasil et al. [13]. Brasil et al. used the test rig at the University of Nottingham shown in Figure 5. In this rig, due to the cost of oil, water is used to model the two phase flow. The air and water are pumped in separately and combined using a T-junction. The flow then reaches a bend in the inlet pipe where it is directed into the de-aerator [13].

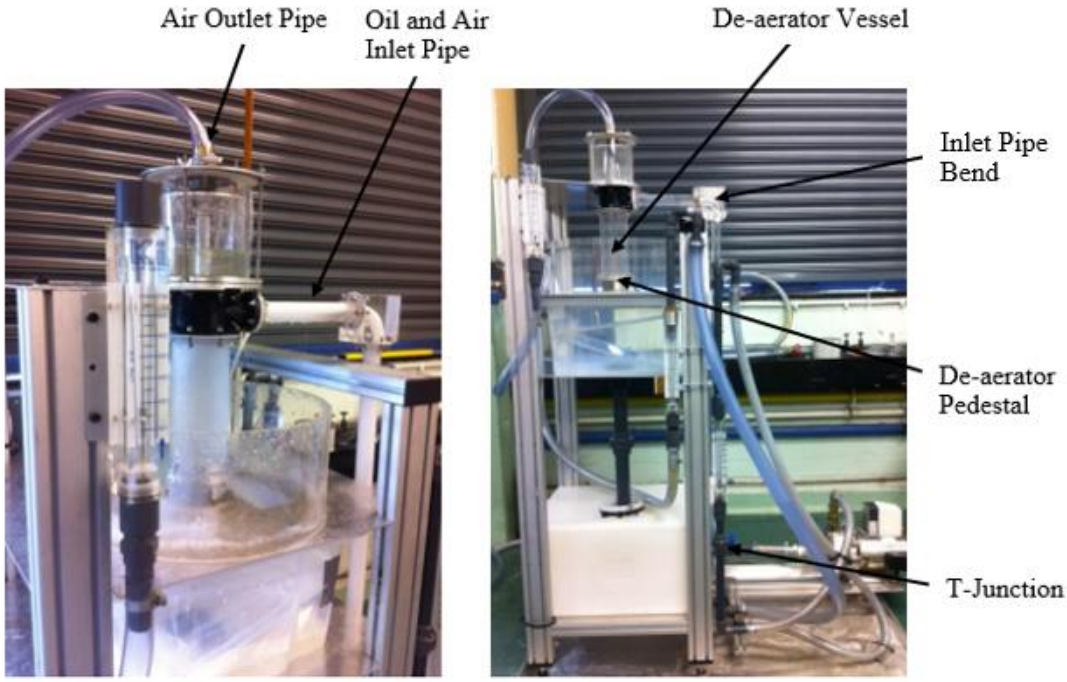

Figure 5: The de-aerator test rig at the University of Nottingham.

Brasil et al. conducted tests to determine the effect of the inlet pipe configuration, the bend radius of the inlet pipe, and the pedestal gap. The inlet pipe configuration was either vertical, horizontal, or 45 degrees. The band radius varied as either half the radius of the inlet pipe, the same radius as the inlet pipe, or double the radius of the inlet pipe. Lastly, a flat pedestal was used with a gap of 7.1%, 8.3%, or 10.7% of the de-aerator radius.

Due to non-disclosure agreement (NDA) restrictions, the exact geometry of the vessel cannot be stated [13].

Additionally, Brasil et al. tested various scavenge ratios by changing the air and water flowrates on the test rig. Brasil concluded that by changing the flow rates and inlet pipe configuration the type of two phase flow changed, with most flows in the vertical inlet pipe being annular dispersed and most flows in the horizontal pipe being intermittent slug or plug flow [13].

Figure 6 shows the water efficiency of the de-aerator rig at a constant water flow rate of 75 L/min [13]. As evidenced in the graph, the efficiency varies heavily depending on the flowrate of air in the system with higher air flow rates reducing the efficiency. This is because the higher flowrates produce more turbulence which shear more water droplets from the film. Additionally, the pedestal gap was shown to have an effect on the efficiency, with the 7.1% results all having lower efficiencies. The efficiency is measured according to Equation 1.2 [13].

$$WE = \frac{\dot{m}_{lv}}{\dot{m}_{inl}} = \frac{\dot{m}_{inl} - \dot{m}_{av}}{\dot{m}_{inl}} \tag{1.2}$$

In Equation 1.2, WE is the water efficiency, m_{lv} is the mass of water that exits through the liquid vent, m_{inl} is the mass of water that enters the de-aerator, and m_{av} is the mass of water that exits through the air vent.

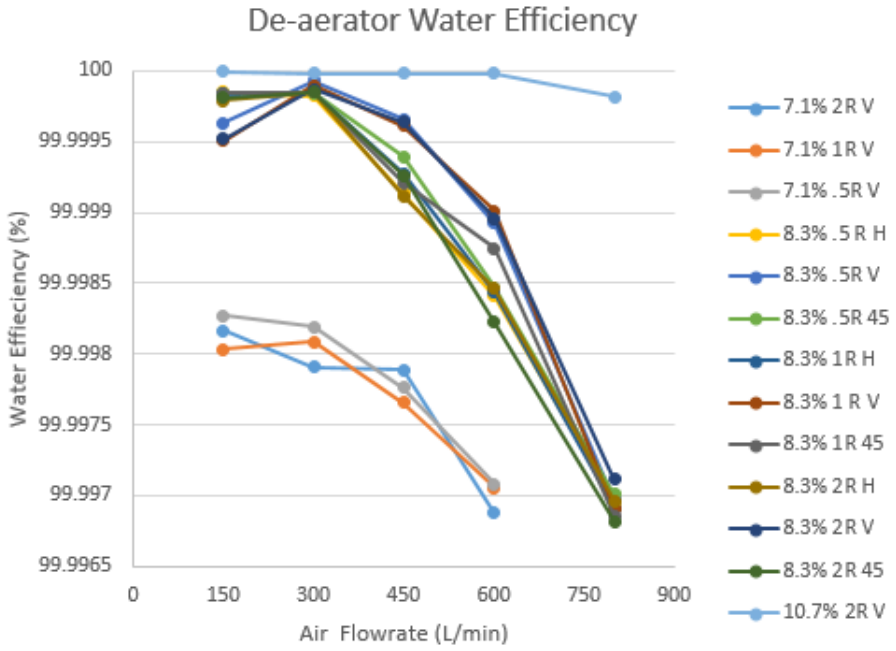

Figure 6: The water efficiency for the de-aerator rig with different inlet configurations and pedestal gaps [13].

While the water efficiency within the system all appear to be very high, well above 99%, this inefficiency can result in possibly hundreds of liters of oil lost on a flight [13]. Therefore, maximizing the efficiency is very important. Brasil et al. results appear to show that the larger the de-aerator gap the higher the efficiency. This is because a larger gap allows for reduced oil pooling on the surface of the de-aerator. However, Brasil's et al results do not show the amount of air that escapes through the liquid vent which is another source of inefficiency for the system.

Following up on Brasil's et al. [13] tests, Nguyen et al. tested different pedestal geometries [14]. Nguyen used the same experimental test rig as Brasil et al. Additionally, Nguyen et al. did not vary the air and water flowrates within the system and instead used a constant 300 (L/min.) of air and 70 (L/min.) of water. Nguyen et al. used pedestal gaps of 7.1%, 8.3%, 9.5%, and 10.7%. Additionally, she also changed the shape of the pedestal using a flat pedestal, a conical pedestal of 15°, and a conical pedestal of 30°.

Figure 7 shows the results of Nguyen et al. tests with the pedestal gap on the X axis and the amount of water exiting through the top hole on the Y axis [14]. This amount of water is the water inefficiency in the de-aerator. Nguyen's et al. results shows that the larger pedestal gaps produce less water inefficiency in the de-aerator. Additionally, the conical pedestals produced significantly less water inefficiency at the smaller pedestal gaps but had less of an impact at the higher pedestal gaps. This is because pooling only occurs at the lower pedestal gaps. The pedestals reduce the surface area of the pool exposed to the air allowing for less shearing of droplets to take place. However, at the larger pedestal gaps, there is no pooling which takes places so the conical pedestal have less of an effect. Similar to Brasil et al., Nguyen's et al. results do not show the amount of air which escapes through the liquid vent. In order to study this, CFD simulations are needed.

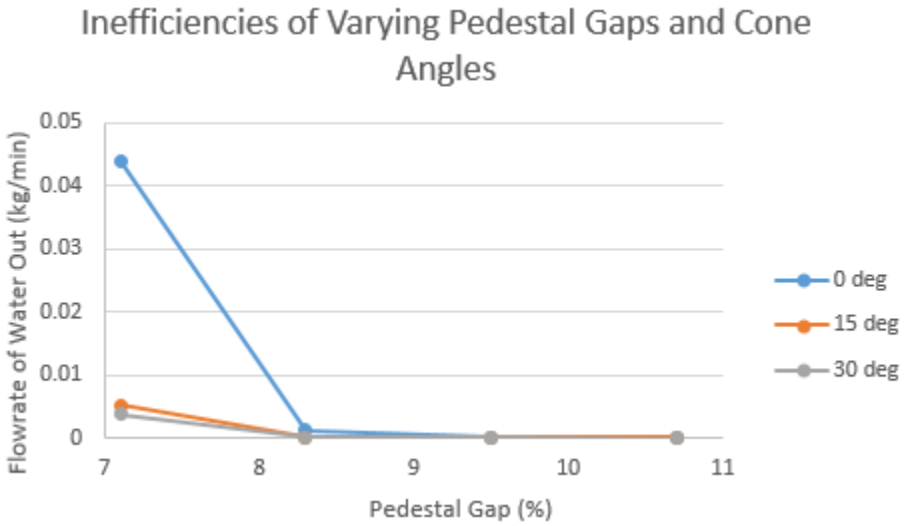

Figure 7: The de-aerator inefficiencies conducted by Nguyen using flat and conical pedestal [14].

Previous CFD simulations have been conducted by Morvan et al. [11]. Morvan et al. studied a previous de-aerator design used in the Rolls Royce Trent XWB. Morvan et al. differed the designs of the de-aerator by changing these parameters:

1. Presence of a pedestal (with and without)
2. Two different De-aerator heights (233% and 365% of the de-aerator radius)
3. Different positions for the liquid vent (De-aerator side and bottom)
4. Different Flight Conditions (Max Takeoff, Cruise, and Ground Idle)

Morvan et al. measured the effectiveness of the de-aerator by measuring the pressure difference between the inlet pipe and the air outlet vent with a larger pressure difference indicating better phase separation [11]. Additionally, Morvan used the Discrete Phase Model (DPM) to model the two phase flow within the de-aerator. Lastly, Morvan et al. modeled annular flow in the de-aerator inlet.

Morvan et al. concluded that the height of the de-aerator had the greatest effect on the pressure difference, with the 365% of the diameter height having the largest pressure differential. This is because it gave the mixture a greater length to separate over. In the cases where a pedestal was present, Morvan et al. concluded that the DPM was not sufficient enough to model the oil film thickness as the high liquid load pushed the DPM to its limits [11]. Therefore, in all further studies, a Volume of Fluid (VOF) method is used.

In a follow up to both Morvan et al. [11] and Brasil et al. [13], Ahmed [6] performed CFD simulations on the de-aerator setup. Ahmed used VOF method to model the two phase flow; two different pedestal gaps were used, 7.1% and 14.2% of the de-aerator radius. Both pedestals were flat. However, due to the large mesh size needed to run these cases, the computation time was very high. Because of this, Ahmed's simulation were not able to reach full completion. Nevertheless, valuable information can still be gained from the results.

Figure 8 shows the film thickness for the 7.1% gap case. While the results for the case were not able to run to completion. As shown in Figure 8, the results varied drastically depending on the circumferential position from which the thickness was measured. The average film thickness was measure to be 22.9% of the radius. Therefore, Ahmed recommended that the pedestal gap be 22.9% of the radius [6]. However, Ahmed measured the thickness of the pooling oil as well in these results. This increased the film thickness as the oil pooled over time and does not accurately represent the appropriate pedestal gap for the de-aerator.

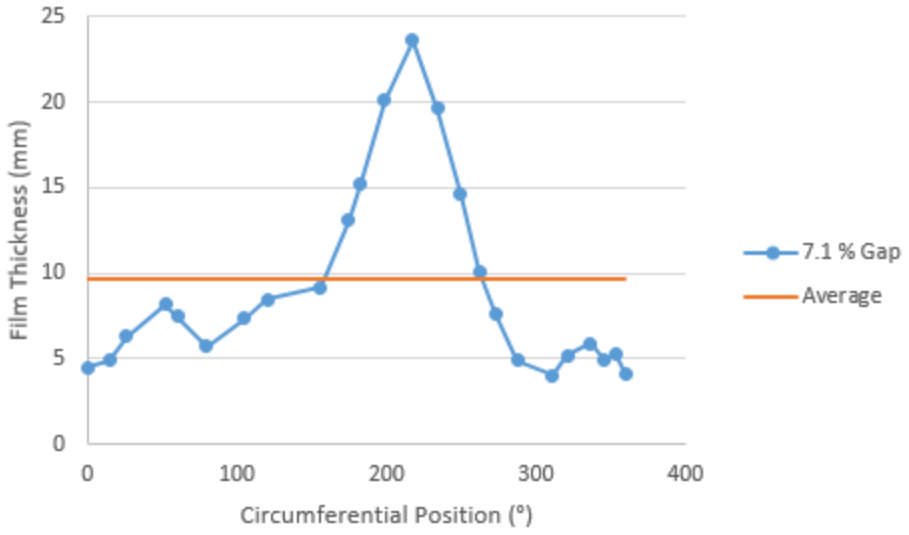

Figure 8: The film thickness in mm at the pedestal for the 7.1 % gap case [6].

For Ahmed's second case of a 14.2% gap, the simulation unfortunately was not able to run to completion or until the pedestal gap filled with water. Therefore no usable results could be obtained from this simulation [6].

1.3.2 De-aerator Objectives

While the de-aerator design is simple, the flows with in the de-aerator are highly complex. The flow is two phase, highly turbulent, and has counteracting vortexes, with the oil flowing down the side of the de-aerator and the air spinning down and then reversing back up and out of the air vent. Currently, due to the complex nature of the flow, no experimental data on the oil film thickness currently exist for the de-aerator. Therefore, CFD will be used to study the flow with the flowing objectives:

1. Use CFD with VOF to study the two phase flow within a de-aerator and calculate the liquid film thickness.
2. Test different conical pedestal with 30° slant and 10.7% gap.
3. Create slug flow at the de-aerator inlet.

1.4 Two-Phase Flow in the De-aerator Inlet Pipe

As the oil and air mixture leaves the bearing chambers and gearboxes, it is combined into to one pipe. The air and oil mixture then flow into the de-aerator. Since the flow entering the de-aerator is a two phase flow, there are multiple configurations which the liquid and gas can be configured. Figure 9 shows different types of two phase flow within a horizontal pipe [15]. Blue represents the liquid flow and white represents the gaseous flow. There are multiple factors which determine the type of two phase flow in a

pipe including, the flowrate of the liquid and gas, the density of the liquid and gas, the orientation of the pipe and the other properties of the liquid and gas [16].

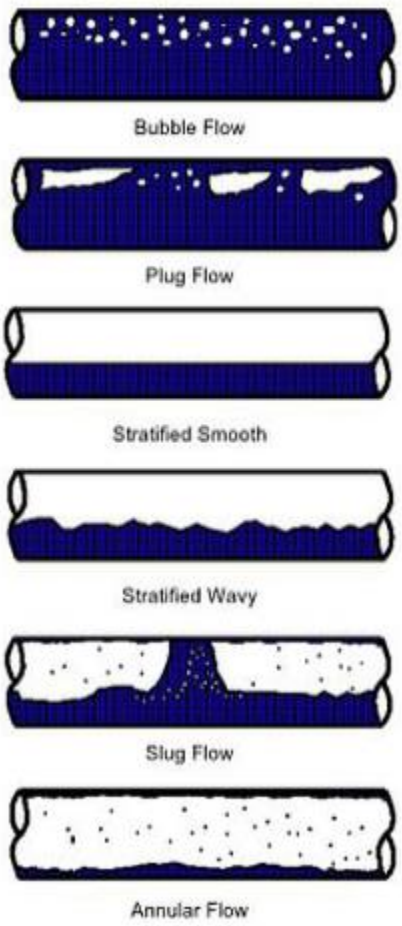

Figure 9: Various types of two phase gas and liquid flow within a horizontal pipe [14].

Figure 9 shows higher flowrates of liquid compared to gas in upper figures and higher flowrates of gas compared to liquid in the lower figures. Bubble flow is comprised predominantly of liquid flow with a small amount of gas flow in the form of bubbles in the liquid [15]. Plug flow is similar to bubble flow in that the flow is predominantly liquid, however there is an increased amount of gas in the flow. This causes a portion of the smaller bubbles to join into a larger bubble. Smaller bubbles are still dispersed in between the larger bubbles [15]. Stratified flow, stratified wavy flow and slug flow are all comprised of similar amounts of liquid and gas flow. Stratified flow shows clear distinction between the liquid and gas phases with the liquid flow at the bottom of the pipe and the gas flow at the top of the pipe. In stratified flow, both gas and liquid flow appear to be laminar producing a smooth interface between the two flows [15]. In stratified wavy flow, there is a clear distinction between the gas and air flow. However, the flow of the gas appears to be turbulent which shears the top of the liquid flow producing waves on the surface of the liquid. Slug flow is similar to plug flow; however, there is a larger percentage of gas in the two phase flow. This creates larger and longer bubbles in the flow with distinct

walls of liquid separating the bubbles [17]. Lastly, annular is comprised primarily of air. There is a small percentage of liquid flow at the base of the pipe. Additionally, small droplets of liquid may be carried in the gaseous flow.

Two phase flow regimes have been studied by researchers including Taitel et al. [18], Madhane et al. [19], and Weisman et al [20]. These researchers have studied two phase flow regimes using experimental data and plotted their results on flow pattern maps. Figure 10 shows the flow pattern map created by Weisman et al [20]. Weisman et al. studied air and water flow in a horizontal pipe with a diameter of 25.6 mm. The flow results were plotted graphically with the liquid superficial velocity on the X axis and the gas superficial velocity on the Y axis.

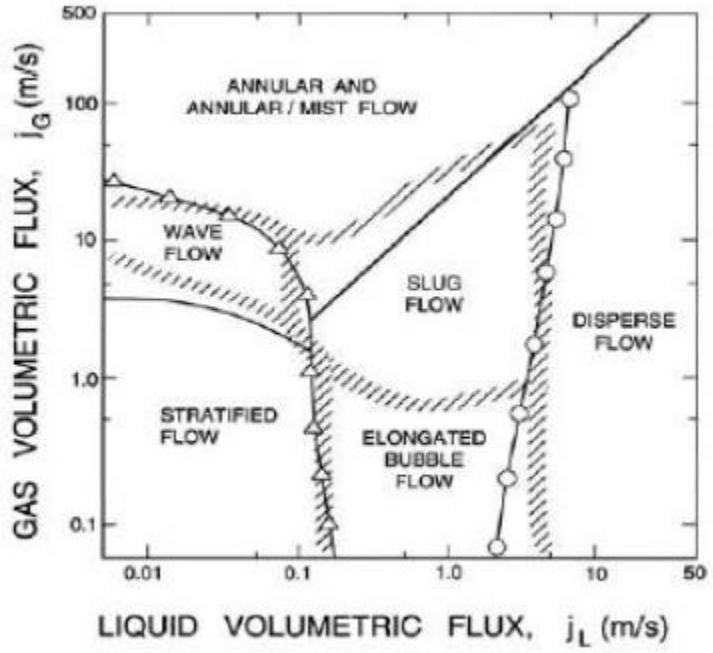

Figure 10: Two phase flow characteristics for air and water in 25.6 mm pipe [19].

1.4.1 Inlet Pipe Previous Research

Using the experimental rig at the University of Nottingham, Brasil et al. determined that for horizontal pipe configurations, the flow into the de-aerator was primarily intermittent slug and plug flow for a variety of air and water flowrates [13]. However, for the vertical pipe geometry, the flow was found to be a dispersed annular flow. Additionally, Nguyen was able to confirm these results using a high speed camera [14].

In order to provide a more accurate CFD simulation, the slug flow needs to be modeled at the inlet. Ahmed researched ways to model slug flow at the inlet. Ahmed conducted three different simulations to attempt to achieve slug flow, patching water film to the edge of the pipe, sending a wave through an annular flow in the pipe, and using a T junction to mix the air and water [6]. The only simulation that was able to successfully

achieve slug flow was the T junction. Ahmed's T junction completed its simulation in 89,000 time steps. The T junction can be seen in Figure 11. This is the same technique used to achieve slug flow in the experimental rig at the University of Nottingham. Ahmed recommended using a T junction to model the slug for the de-aerator inlet. While this T junction achieved slug flow, it took high computational time due to the abrupt change in momentum of the air.

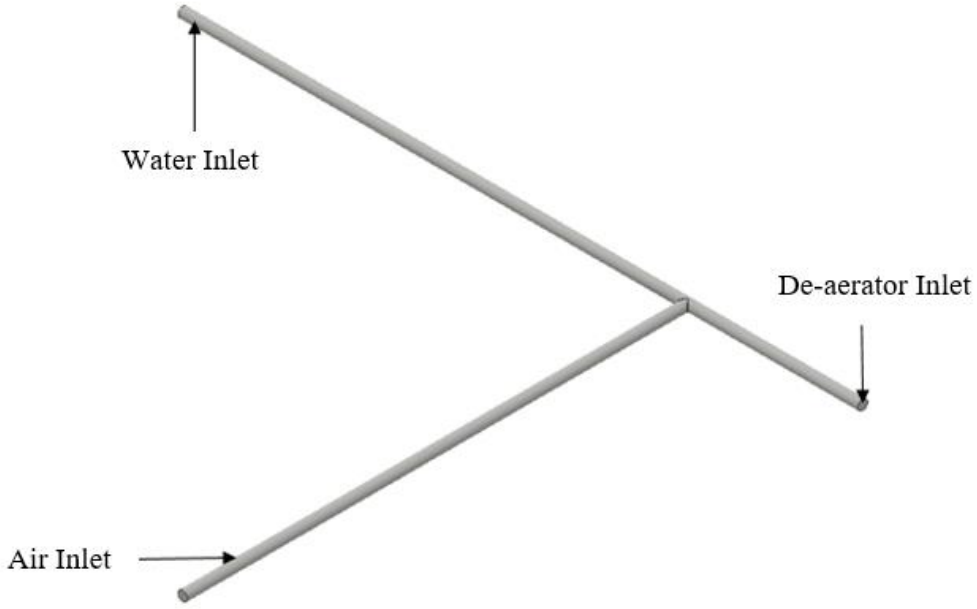

Figure 11: The T junction used by Ahmed to achieve slug flow [6].

1.4.2 Inlet Pipe Objectives

The flow in to the de-aerator has been shown to be slug flow at ground idle engine conditions. Ground idle conditions have shown to produce the most inefficiency within the engine. Therefore, in order to better replicate the flow within the de-aerator at ground idle conditions, slug flow should be modeled at the the inlet. However, slug flow can vary depending on the frequency and size of the air bubbles. Thus, the way in which slug is achieved is important to determine the flow within the de-aerator. Previous research both experimentally and through CFD, shows that slug flow can be achieved through a T junction with the liquid and gas entering at separate inlets, mixing, and exiting through a singular outlet. Conversely, this case required high computation time due to the abrupt change in momentum of the air [6]. Consequently, for this research, a Y junction will be used with the liquid and gas at separate inlets with the following objectives:

1. Use Y junction to achieve slug flow at flowrates of 70 and 150 (L/min.) and 70 and 300 (L/min) of air and water respectively.

2.0 Methodology

This section will discuss the mathematical equations used to calculate the results of the CFD simulation. The governing equations of CFD will be shown, as well as the turbulence and two phase flow equations necessary to calculate the highly turbulent and complex two phase flow within the bearing chamber and de-aerator.

2.1 Governing Equations

Fluid flow can be described by three governing equations: the continuity equation, the momentum equations, and the energy equation. These equations can be derived using the laws of conservation of mass, momentum, and energy and applying them to a finite control volume [21]. In this research, the energy equation does not apply.

2.1.1 Continuity Equation

The continuity equation is derived from law of conservation of mass and is shown in Equation 2.1.

$$\frac{\partial \rho}{\partial t} + \frac{\partial (\rho u)}{\partial x} + \frac{\partial (\rho v)}{\partial y} + \frac{\partial (\rho w)}{\partial z} = 0 \tag{2.1}$$

Where ρ is the density, t is time, and u, v, and w are the x, y, and z components of velocity respectively. The equation states that net mass flow out of the control volume must be equal to the time rate of decrease in mass inside the control volume [21]. If the simplifying assumption of incompressible flow can be made, then the continuity equation reduces.

$$\rho \frac{\partial u}{\partial x} + \rho \frac{\partial v}{\partial y} + \rho \frac{\partial w}{\partial z} = 0 \tag{2.2}$$

Equation 2.2 states that the flowrate into the control volume must equal the flowrate out of the control volume.

2.1.2 Momentum Equation

The momentum equations are derived similarly to the continuity equation except using the law of conservation of momentum. This law is Newton's second law.

$$F = ma \tag{2.3}$$

Newton's second states that when a force is applied to an object with mass, the momentum of that object will change. By applying this principle to a finite control volume, we derive the momentum equations for the x, y, and z components of the flow [21].

X: $$\frac{\partial(\rho u)}{\partial t} + \frac{\partial(\rho u^2)}{\partial x} + \frac{\partial(\rho uv)}{\partial y} + \frac{\partial(\rho uw)}{\partial z} = -\frac{\partial P}{\partial x} + \frac{\partial \tau_{xx}}{\partial x} + \frac{\partial \tau_{yx}}{\partial y} + \frac{\partial \tau_{zx}}{\partial z} + \rho f_x \tag{2.4}$$

Y: $$\frac{\partial(\rho v)}{\partial t} + \frac{\partial(\rho uv)}{\partial x} + \frac{\partial(\rho v^2)}{\partial y} + \frac{\partial(\rho vw)}{\partial z} = -\frac{\partial P}{\partial y} + \frac{\partial \tau_{xy}}{\partial x} + \frac{\partial \tau_{yy}}{\partial y} + \frac{\partial \tau_{zy}}{\partial z} + \rho f_y \tag{2.5}$$

Z: $$\frac{\partial(\rho w)}{\partial t} + \frac{\partial(\rho wu)}{\partial x} + \frac{\partial(\rho wv)}{\partial y} + \frac{\partial(\rho w^2)}{\partial z} = -\frac{\partial P}{\partial z} + \frac{\partial \tau_{xz}}{\partial x} + \frac{\partial \tau_{yz}}{\partial y} + \frac{\partial \tau_{zz}}{\partial z} + \rho f_z \tag{2.6}$$

Where τ is the shear stress acting on a surface of the control volume, P is the pressure acting on the control volume, and f is any additional force. Equations 2.4, 2.5, and 2.6 are known as the Navier-Stokes Equations because they were developed independently by Navier and Sir George G. Stokes [21]. If flow can be considered incompressible, then equations will reduce to a simpler form.

X: $$\rho \frac{\partial u}{\partial t} = -\frac{\partial P}{\partial x} + \mu\left(\frac{\partial^2 u}{\partial x^2} + \frac{\partial^2 u}{\partial y^2} + \frac{\partial^2 u}{\partial z^2}\right) + \rho f_x \tag{2.7}$$

Y: $$\rho \frac{\partial v}{\partial t} = -\frac{\partial P}{\partial y} + \mu\left(\frac{\partial^2 v}{\partial x^2} + \frac{\partial^2 v}{\partial y^2} + \frac{\partial^2 v}{\partial z^2}\right) + \rho f_y \tag{2.8}$$

Z: $$\rho \frac{\partial z}{\partial t} = -\frac{\partial P}{\partial z} + \mu\left(\frac{\partial^2 w}{\partial x^2} + \frac{\partial^2 w}{\partial y^2} + \frac{\partial^2 w}{\partial z^2}\right) + \rho f_z \tag{2.9}$$

2.2 Numerical Methods to solving Differential Equations

While the governing equations of fluid dynamics cannot be solved analytically, the results can be approximated through discretizing the governing equations. The governing equations assume conservation of mass, momentum, and energy over an infinitesimally small control volume through discretizing the equations, the same principles can be applied over a physical control volume [22]. Therefore, by dividing the entire geometry into small control volumes, the solutions to the governing equations can be approximated accurately. In CFD these control volumes are called cells, and the solutions to the governing equations are constant across the cells. The center of each cell is called a node, and this is the location

where the governing equations are solved [21]. There are multiple different techniques for discretizing including: finite difference method (FDM), finite volume method (FVM), finite element analysis (FEA), and boundary element analysis (BEA). For this research, finite volume method is used.

When the continuity and Navier-Stokes equations are discretized, Equations 2.10 and 2.11 are produced respectively.

$$p_{i,j}^{n+1} = p_{i,j}^{n} - \Delta t \left[\rho \frac{u_{i+1,j,k}^{n} - u_{i-1,j,k}^{n}}{2\Delta x} + \rho \frac{v_{i,j+1,k}^{n} - v_{i,j-1,k}^{n}}{2\Delta y} + \rho \frac{w_{i,j,k+1}^{n} - w_{i-1,j,k-1}^{n}}{2\Delta z} \right] \tag{2.10}$$

$$\begin{aligned} u_{i,j}^{n+1} = u_{i,j}^{n} - \frac{\Delta t}{\rho} \Bigg[& \rho u_{i,j}^{n} \frac{u_{i+1,j,k}^{n} - u_{i-1,j,k}^{n}}{2\Delta x} + \rho v_{i,j}^{n} \frac{u_{i,j+1,k}^{n} - u_{i,j-1,k}^{n}}{2\Delta y} + \rho w_{i,j}^{n} \frac{u_{i,j,k+1}^{n} - u_{i,j,k-1}^{n}}{2\Delta z} \\ & + \frac{p_{i+1,j,k}^{n} - p_{i-1,j,k}^{n}}{2\Delta x} - \mu \frac{u_{i+1,j,k}^{n} - 2u_{i,j,k}^{n} + u_{i-1,j,k}^{n}}{\Delta x^{2}} \\ & - \mu \frac{u_{i,j+1,k}^{n} - 2u_{i,j,k}^{n} + u_{i,j-1,k}^{n}}{\Delta y^{2}} - \mu \frac{u_{i,j,k+1}^{n} - 2u_{i,j,k}^{n} + u_{i,j,k-1}^{n}}{\Delta z^{2}} \Bigg] \end{aligned} \tag{2.11}$$

In Equations 2.10 and 2.11, Δx, Δy, and Δz are the distances between each node in the x, y, and z directions. Additionally, i, j, and k are the labels for each node in the x, y, and z direction respectively. Lastly n is the label for each time iterations and Δt is the time between each time iterations. A time iteration is the process by which the governing equations are discretized through time. Similarly, to discretizing the equations spatially as long as the amount of time between each time step is small, the solution to the equations can be approximated accurately [21].

In order to determine what size time step should be used, the Courant-Fredichs-Lewy (CFL) method is used and shown in Equation 2.12 [23].

$$CFL = \frac{c\Delta t}{\Delta x} \tag{2.12}$$

This equation Δx is the distance between nodes and c is the magnitude of the velocity. For most simulations, the CFL should be kept at or below 1. However, for more complex simulations, it may be necessary to assume a smaller CFL. For the purpose of this research, the time step has been calculated assuming a CFL of .3 for the de-aerator and slug flow simulations and a CFL of 1 for the bearing chamber simulations.

2.3 Turbulence Models

Turbulent flow can be characterized by the fluctuating agitated velocity flow field. This viscous forces of the flow are small compared to the velocity forces. This leads to destabilizations within the flow and creates the unsteady eddies associated with turbulent

flow [24]. Turbulent flow can be characterized by two values, the mean velocity, $U_i(x_k)$, of the flow and the velocity of the fluctuations of the flow, $u'(x_k, t)$.

$$u_i(x_k, t) = U_i(x_k) + u'(x_k, t) \tag{2.13}$$

In order to solve the turbulent flow equation, 2.13 can be substituted in the continuity and Naiver-Stokes equations. However, the presence of the velocity fluctuation term creates an additional variable to be solved for. This provides more variables than equations. Therefore, an additional equation is required to solve. This equation is the Reynolds Average Navier Stokes equation (RANS). This is the basis for most turbulence models [25].

$$U_i(x_k) = \lim_{T\to\infty} \frac{1}{T} \int_0^T u(x_k, t)dt \tag{2.14}$$

$$U_j \frac{\partial U_i}{\partial x_j} = -\frac{1}{\rho}\frac{\partial P}{\partial x_i} + \frac{\partial}{\partial x_j}\left(\frac{\mu}{\rho}\frac{\partial U_i}{\partial x_j}\right) + \frac{\partial(-\overline{u_i' u_j'})}{\partial x_j} \tag{2.15}$$

Equation 2.14 is the time average of the velocity across the entire simulation time. Equation 2.15 is the RANS equation. In the equation, U is the average velocity and $\frac{\partial(-\overline{u_i' u_j'})}{\partial x_j}$ represents the velocity fluctuation term and is known as the Reynolds stresses. Boussinesq determined that the Reynolds stresses were directly related to unsteadiness of the flow [26]. Boussinesq characterized this unsteadiness as the turbulent viscosity, μ_t. These relations can be seen in Equations 2.16 and 2.17

$$-\overline{u_i' u_j'} = 2\frac{\mu_t}{\rho} S_{i,j} \tag{2.16}$$

$$S_{i,j} = \frac{1}{2}\left(\frac{\partial U_i}{\partial x_j} + \frac{\partial U_j}{\partial x_i}\right) \tag{2.17}$$

Modeling the turbulent viscosity term is basis for most turbulent models, including the Spalart-Allmaras, k-ε, and k-ω models.

2.3.1 SST k-ω Model

Two of the primary turbulence models are k-ε and k-ω. The k-ε model is a first order equation and, therefore, less computationally expensive. However, the k-ε model is also less accurate. This is especially true in the near wall regions of the flow where k-ε method tends to fail [24]. The k-ω model, however, is a second order equation and, therefore, more accurate and stable. However, since k-ω is a second order equation, it is more computationally expensive to run.

The shear stress transport (SST) k-ω model was developed by Menter combines the benefits of both k-ω and k-ε model [27]. The SST k-ω uses the k-ω equations in the near wall regions of the mesh where k-ε fails. Additionally, the model uses k-ε in the free stream velocities in order to save computation time.

The SST k-ω model is also superior for separated flows similar to what is seen in the de-aerator. However, the SST k-ω model can produce large turbulence values in regions of high normal strain. Therefore, a damping equation is needed. In this research, the SST k-ω model with turbulence damping is used.

The Equations 2.18 and 2.19 show the SST k-ω model. Equation 2.18 is the turbulent kinetic energy equation and defines k while Equation 2.19 is the specific dissipation equation and defines ω.

$$\frac{\partial k}{\partial t} + U_j \frac{\partial k}{\partial x_j} = P_k - \beta k\omega + \frac{\partial}{\partial x_j}[(v + \sigma_k v_T)\frac{\partial k}{\partial x_j}] \tag{2.18}$$

$$\frac{\partial \omega}{\partial t} + U_j \frac{\partial \omega}{\partial x_j} = \alpha S^2 - \beta \omega^2 + \frac{\partial}{\partial x_j}\left[(v + \sigma v_T)\frac{\partial \omega}{\partial x_j}\right] + 2(1 - F_1)\sigma_\omega \frac{1}{\omega}\frac{\partial k}{\partial x_i}\frac{\partial \omega}{\partial x_i} + \delta_i \tag{2.19}$$

In Equations 2.18 and 2.19, P_k, β, and σ_ω are all constants defined by the solver. In Equation 2.19, δ_i is the damping source term used for turbulence damping. For a more detailed explanation of the turbulence model, please refer to [28]. These two equations fix the closure problem and allow for the turbulent velocity to be solved.

2.3.2 Turbulence Damping

As stated previously turbulence damping is necessary in these simulations to reduce the high turbulence values that can be caused by the SST k-ω model. Therefore, the damping source term was added into Equation 2.19 by Egroov [29]. Equation 2.20 shows the equation for the turbulence damping source term.

$$\delta_i = A_i \Delta n \beta \rho_i \left(\frac{6B\mu_i}{\beta \rho_i \Delta n^2}\right)^2 \tag{2.20}$$

In Equation 2.20, B is the damping constant, A_i, is the interfacial area density, ρ_i is the density of phase i, Δn is the cell height normal to the surface, and β is a predetermined coefficient. The damping constant is a number between 0 and 100. A damping constant of 80 is used for this research. A_i can be calculated using Equation 2.21. The interfacial area can be calculated using Equation 2.21.

$$A_i = 2\alpha_i |\Delta \alpha_i| \tag{2.21}$$

2.4 Two-Phase Flow Modeling

In Fluent, many approaches can be used to determine the results of two phase flow simulations. All cases can be divided into two sections: Euler-Lagrange and Euler-Euler. In the Euler-Lagrange methods, one phase is continuous and the other phases are all considered discrete. However, in the Euler-Euler methods, all phases are considered continuous. In Fluent, one can choose Volume of Fluid (VOF), Mixture, or Eulerian.

2.4.1 Volume of Fluid (VOF)

The VOF model is an Euler-Euler model developed by Hirt and Nichols [30]. Therefore, both phases are treated as continuous phases. The VOF method works by calculating the volume fraction in each cell. Then the continuity equation is solved for each phase. The momentum equations, however, are shared amongst all the phases. This allows the fluid properties of each cell to vary depending on the volume fraction of the cell. The fluid properties can be calculated using Equations 2.22, 2.22, 2.24, and 2.25.

$$\alpha_i = \frac{V_i}{V} \tag{2.22}$$

$$\sum \alpha_i = 1 \tag{2.23}$$

$$\rho = \sum \rho_i \alpha_i \tag{2.24}$$

$$\mu = \sum \mu_i \alpha_i \tag{2.25}$$

Equation 2.22 calculates the volume fraction in a cell as the volume of the fluid over the total volume in a cell. Equation 2.23 states that the sum of all the volume fractions must equal one. This helps to conserve mass in the simulation. Lastly, Equation 2.24 and 2.25 calculate the density and viscosity of each cell as the summation of each density or viscosity of each phase multiplied by the volume fraction of that phase.

2.5 Solver

In this research a pressure based solver is used to find the solution to the discretized governing equations. There are two types of pressure based solvers used in Fluent segregated and coupled solvers. Segregated solvers solve each of the governing equations successively. Coupled solvers, however, solve the governing equations simultaneously. A segregated solver is used in this research.

Fluent allows the users to pick from four solution methods Semi-Implicit Method for Pressure Linked Equations (SIMPLE), Semi-Implicit Method for Pressure Linked Equations Consistent (SIMPLC), Pressure Implicit with Splitting of Operators (PISO), and Coupled. Of these methods, SIMPLE is used in this research.

2.5.1 SIMPLE

The SIMPLE works using the process shown in Figure 12 and was developed by Patankar et al. [31]. First, initial values are determined using the values that are initialized for the first time. After the first time step, all initial values are from the previous time step. The discretized momentum equations are then solved. Next, the pressure correction equation is solved, and the pressure and velocity are corrected. These corrected values are then used to solve the transport equations. Lastly, the solution is checked for convergence. If the solution does not converge, the loop repeats with the new pressures and velocities. However, if the solution converges, the simulation takes a time step forward, and the process is then started again.

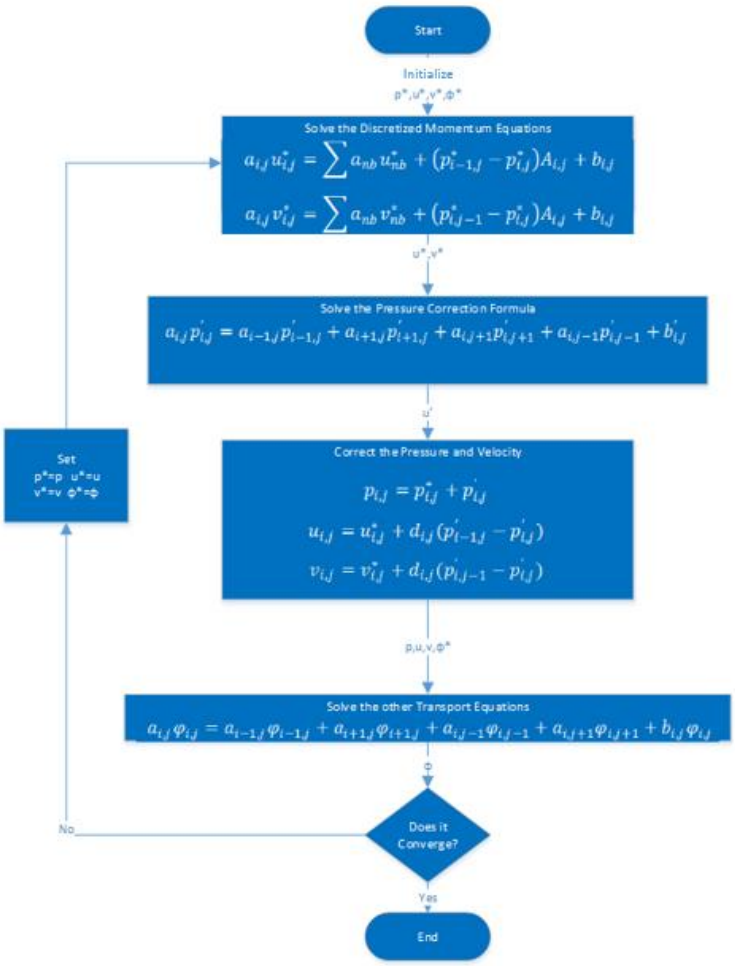

Figure 12: A flowchart diagraming the steps used by the SIMPLE solver.

4.0 Setup and Results

This section will detail the setup and results for all bearing chamber, slug flow, and de-aerator simulations.

4.1 Bearing Chamber

As stated previously, it is important to determine the behavior of the two phase flow within the bearing chamber of a jet engine. By determining where the oil pools within the jet engine bearing chamber, the sump can be better positioned to remove more oil and less air thus reducing the scavenge ratio.

4.1.1 Bearing Chamber Geometry and Mesh

In this research the bearing chamber is modeled as two concentric circles with the flow regime inside the circles as shown in Figure 13. The model is similar to the KIT geometry used by Gorse et al. and Adeniyi [5, 9]. In the geometry, the inner radius is 86.4% of the outer radius. All bearing chamber simulations are 2 dimensional (2D). In all simulations the inner wall rotates at a specified angular velocity while the outer wall remains stationary.

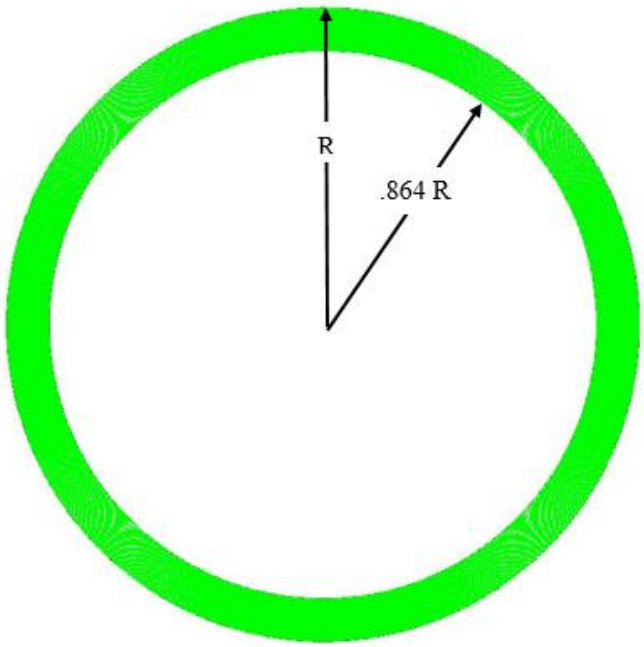

Figure 13: Bearing chamber geometry based on the KIT geometry from the Karlsruhe Institute for Technology.

The mesh for the above geometry is a hexahedral mesh with 118404 cells and 119600 nodes. Figure 14 shows the quality, determinant, and minimum angle respectively for the mesh. In order for the simulation to run properly in Fluent, the minimum quality and determinant has to be above 0.2 and the minimum angle has to be above 14°. As evident by Figure 14, the mesh meets all the criteria and should run successfully in Fluent.

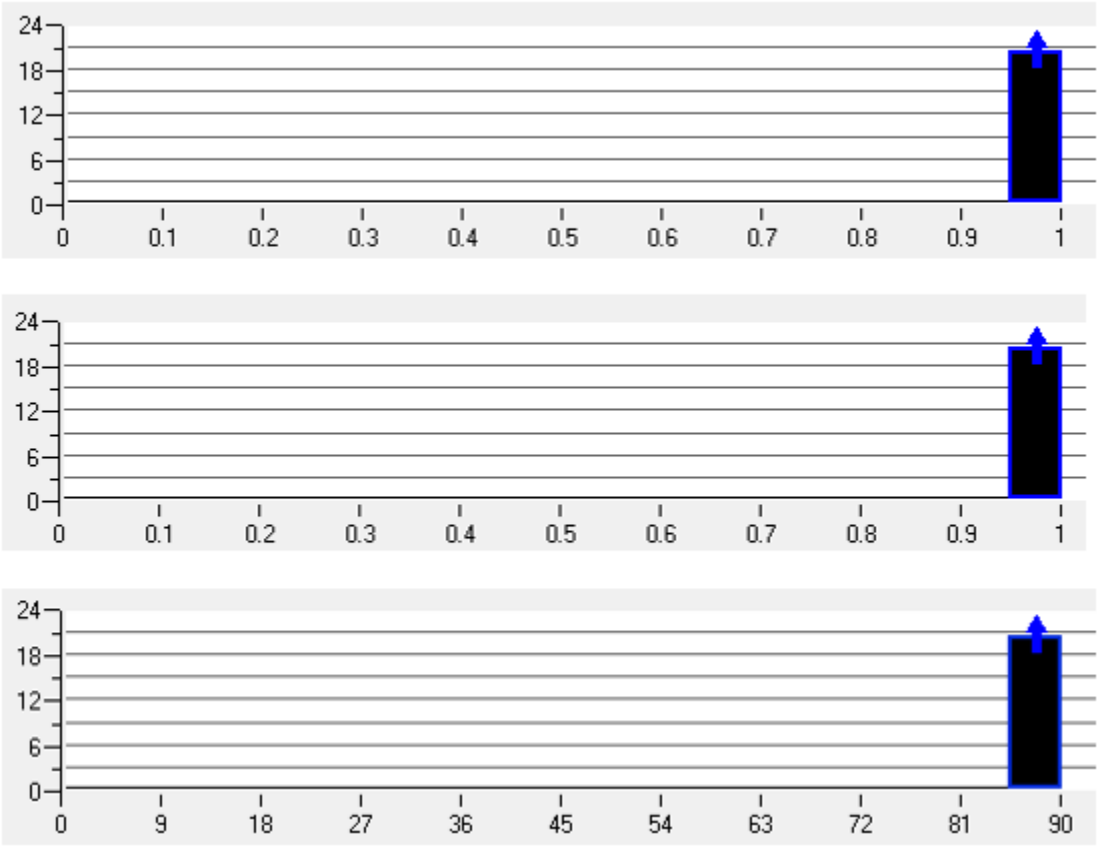

Figure 14: Histograms showing the quality, determinant, and min angle respectively for the bearing chamber mesh.

4.1.2 Bearing Chamber Boundary and Operating Conditions

The bearing chamber is simulated as two concentric circles. The inner circle is modeled after the turbine shaft and, therefore, spins. This spinning is what drives the two phase flow within the bearing chamber. The turbine shaft spins at a multitude of speeds depending on the flight conditions, ground idle, max takeoff, and cruise. Therefore, four simulations were run with a turbine shaft speed of 500, 2000, 4000, and 7000 rpm.

The simulation is initialized first using only air at steady state. Once the simulation reaches convergence, oil is patched into the bottom of the bearing chamber up to a height of 9.45% of the outer radius. This can be seen in Figure 15. The oil is shown in red and the air is shown in blue.

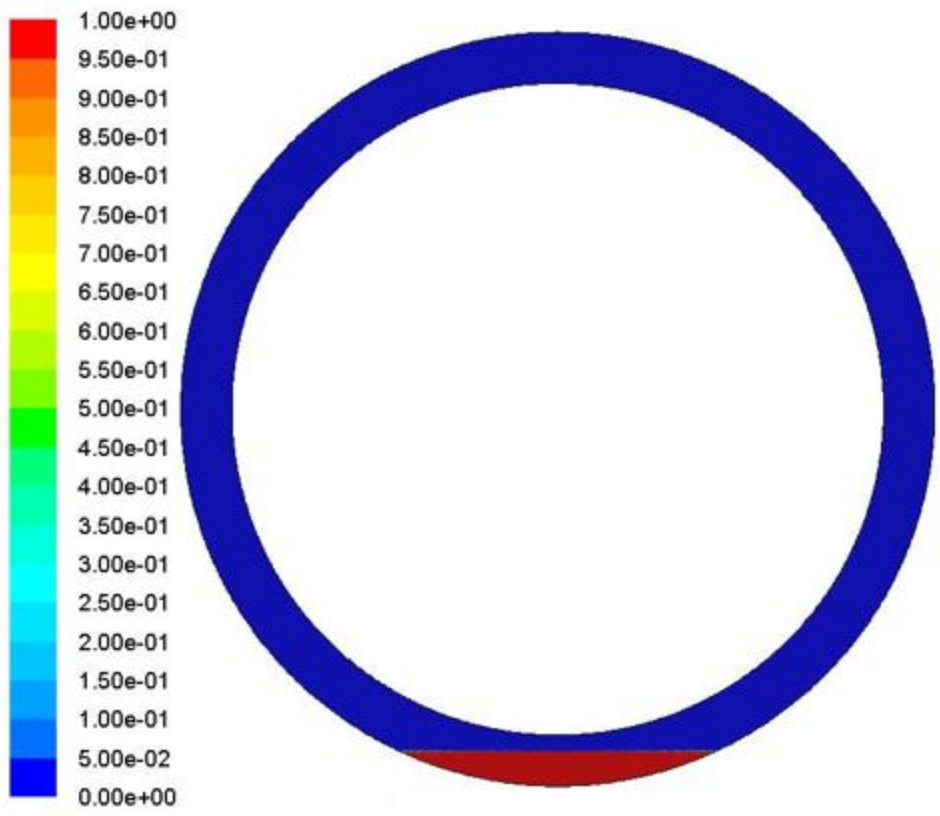

Figure 15: The oil patched into the bottom of the bearing chamber after it is initialized. The volume fraction of oil is shown with the oil displayed in red and air in blue.

For all bearing chamber the following operating conditions are used.

1. Air density is 1.2 kg/m^3
2. Air dynamic viscosity is 1.7894 e-5 kg/m-s
3. Oil density is 886 kg/m^3
4. Oil dynamic viscosity is 4.78 e-2 kg/m-s
5. Gravity is -9.81 m/s^2
6. Surface tension between the air and oil is 0.072 N/m
7. Operating pressure is 101.325 kPa

4.1.3 Bearing Chamber Models and Methods

All bearing chamber simulations are modeled using the VOF model for two phase flow. Additionally, the SST k-ω model is used for turbulence simulation. A damping factor of 80 is applied to the turbulence model. Curvature correction is also applied to the turbulence model.

The SIMPLE method is used to solve the pressure-velocity coupling. A second order upwind discretization technique is used for the momentum, turbulent kinetic energy, and specific dissipation rate. The volume fraction is solved using a compressive technique. Lastly, the time step is solved using a first order implicit scheme. All residuals were said to have converged at a value of 1e-6.

A variable time step is used with a minimum time step of 1e-9 s and a maximum time step of 1e-3 s. The time step is determined so the CFL is 1. The maximum factor of change in the time step is set to 5 and the minimum factor of change is 0.5. The simulation ran until a transient time of 1 s was achieved.

4.1.4 Bearing Chamber Results

The results for all bearing chamber simulations can be seen in Figure 16. Figure 16 shows the contours of the oil volume fraction in the simulation. As can be seen in the figure, as the speed of the turbine shaft increases, the overall volume fraction of the oil decreases. This is most likely caused by the increase in the turbine shaft speed causing the air speed to increase. This, in turn, can then shear particles of oil from the film surface. This causes a misting effect and reduces the volume fraction of the oil. Additionally, refining the mesh could help to provide better resolution into the actual volume fraction of the oil.

As shown in Figure 16, the 2000 rpm turbine case does appear to provide enough air flow to drive the oil. Instead the gravitational force of the oil is stronger than the viscous force of the air, and the oil remains at the base of the bearing chamber. In the 4000 rpm case, however, the gravitational force of the oil and the viscous force of the air appear to be of the same magnitude. This causes some of the oil to pool at the base of the bearing chamber; however, there is still a thin film around the entire bearing chamber wall. Additionally, the oil pools to the left of center. This is due to the air driving the oil in a counter-clockwise motion. Lastly, the 7000 and 14000 rpm cases, both show the viscous air force has overpowered the gravitational force. This causes oil thickness to appear even across the entire bearing chamber.

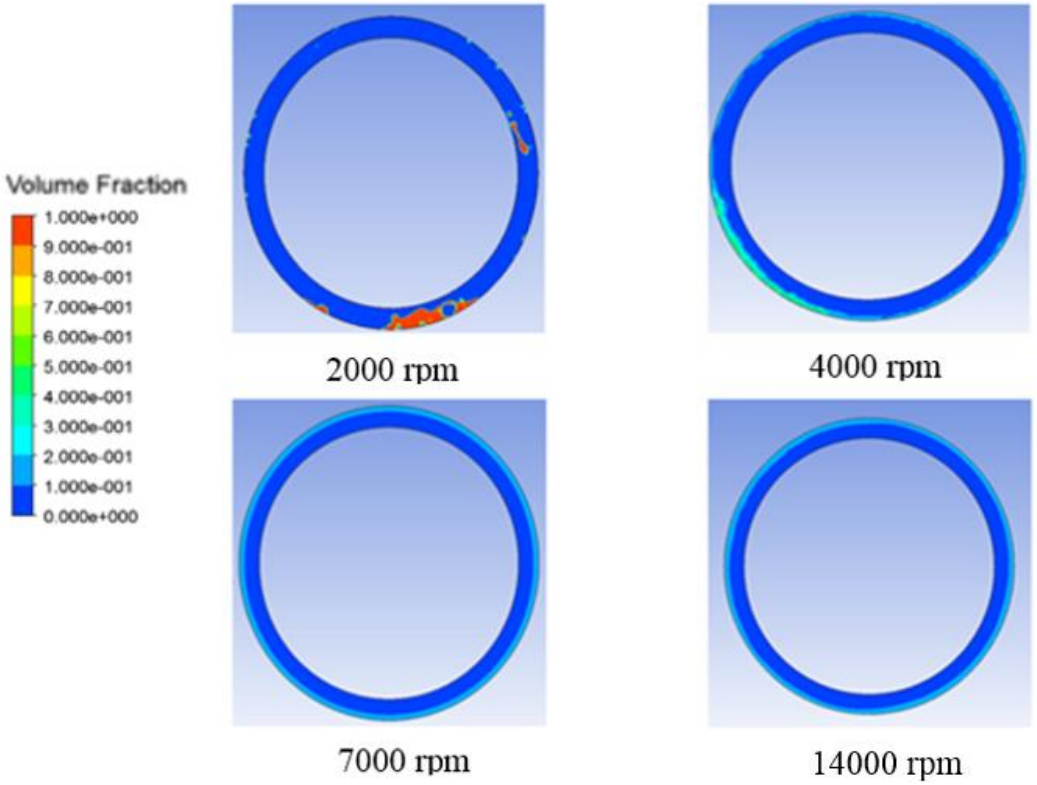

Figure 16: The oil in the KIT after 1 s for the 2000, 4000, 7000, and 14000 RPM cases respectively.

Figure 17 shows the oil film thickness for each of the bearing chamber cases with respect to the circumferential position along the bearing chamber wall. As can be seen for the 2000 rpm case, the oil is pooled in one spot between 260° and 310°. The amount of pooling in the 4000 rpm case is significantly less, however, still noticeable. Additionally, at 7000 and 14000 rpm, the oil thickness appears constant.

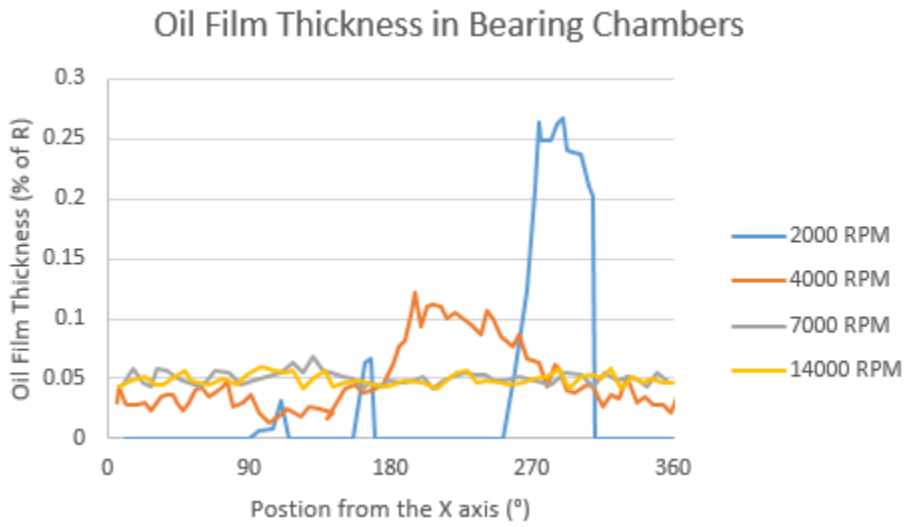

Figure 17: Oil film thickness along the bearing chamber wall with respect to the circumferential position.

4.1.5 Bearing Chamber Conclusion

The bearing chamber houses the ball bearings for the turbine shaft. Oil comes off of the ball bearings and collects on the walls of the bearing chamber. This oil must be recycled out of the bearing chamber. In order to better recycle the oil in the bearing chamber, the two phase flow within the chamber was studied. The flow is driven by the turbine shaft which can operate at variable speeds. Therefore, turbine shaft speeds of 2000, 4000, 7000, and 14000 rpm were studied.

From the results of these simulations, it was discovered that as the turbine shaft speeds increased, the overall volume fraction of the oil decreased. This is a result of the high air speeds shearing droplets of oil off the surface of the oil film. In order to help better identify the oil, a finer mesh is needed. Figure 17 shows that at 2000 rpm, the viscous force of the air is not strong enough to overcome the gravitational force of the oil. This causes the oil to pool at the base of the bearing chamber. Additionally, at 4000 rpm, the viscous force of the air appears of the same magnitude as the gravitational force of the oil. This causes the oil to pool in the bottom left corner of the bearing chamber due to the counter-clockwise motion of the turbine shaft. There is a thin film of oil around the wall of the bearing chamber. Lastly, for the 7000 and 14000 rpm cases, the viscous force of the air is greater than the gravitational force of the oil. This causes the oil to form an even film around the entire bearing chamber.

4.2 Y Junction Slug Flow

In order to achieve a more exact simulation, the flow into the de-aerator needs to better represent the actual inlet flow of the de-aerator. The flow into the experimental rig at the University of Nottingham has been shown to produce slug flow by both Brasil and Nguyen [13, 14]. Ahmed was able to produce slug at the using a T-Junction [6]. While this is the desired flow for the inlet it is computationally expensive. Therefore a Y-junction will be used to attempt to create slug flow. The Y-junction reduces change in momentum for the water and, therefore, should be less computationally expensive.

4.2.1 Y Junction Geometry and Mesh

The Y junction geometry can be seen in Figure 18. Figure 18 shows both the air and water inlet converging to one singular fluid outlet. This fluid outlet will lead to the de-aerator in future simulations. The length of the air and water inlets are 50 times the diameter of the pipe. The fluid outlet is 17.5 times the diameter of the pipe. Water is used in these simulations because it accurately models the properties of oil and is used in the experimental rig at the University of Nottingham.

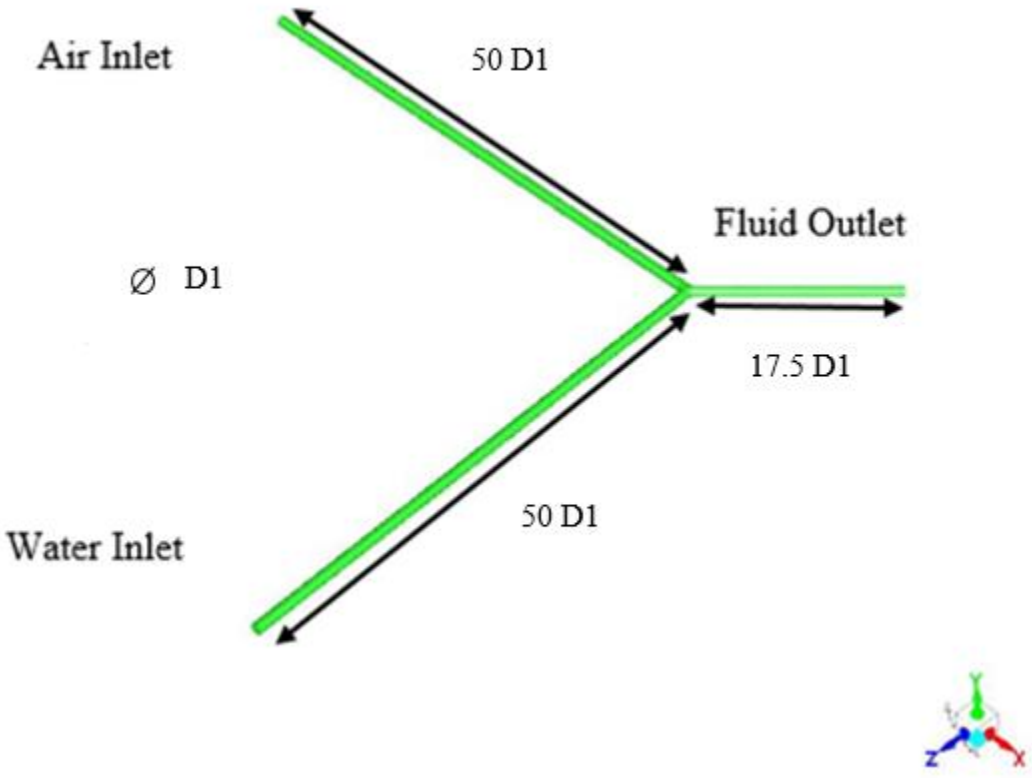

Figure 18: The Y junction geometry. Shows the water and air inlets converging to one outlet.

The mesh for all Y junction simulations was created in ICEM and is a tetrahedral mesh of 581741 cells and 1467619 nodes. A boundary layer was applied to the wall of the Y junction geometry to help resolve the boundary layer flow. The boundary layer is ten cells thick and increases at a ratio of 1.2 starting at the wall. Additionally, the mesh was converted to polyhedral in Fluent. This reduces the computation of the simulation. A cross section of the mesh can be seen in Figure 19. This figure shows the boundary layer inflation at the walls.

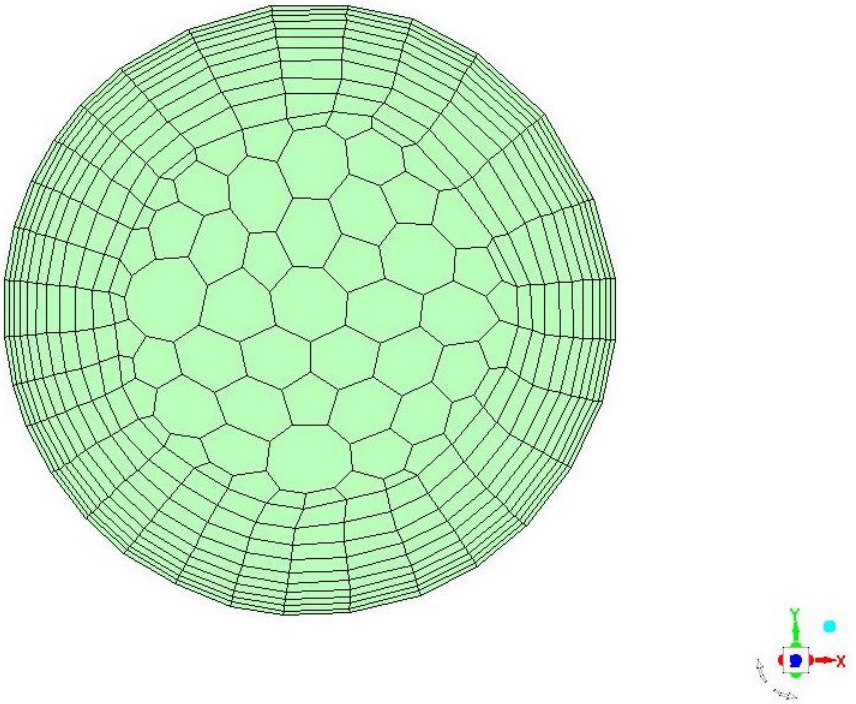

Figure 19: A cross-sectional view of the Y junction mesh showing the boundary layer inflation.

The quality, determinant 3x3x3, and minimum angle respectively can be seen in Figure 20. Both the quality and the determinant meet the minimum mesh requirement of 0.2. The minimum angle for the mesh is 14.64° which is larger than the 14.0° minimum angle recommendation.

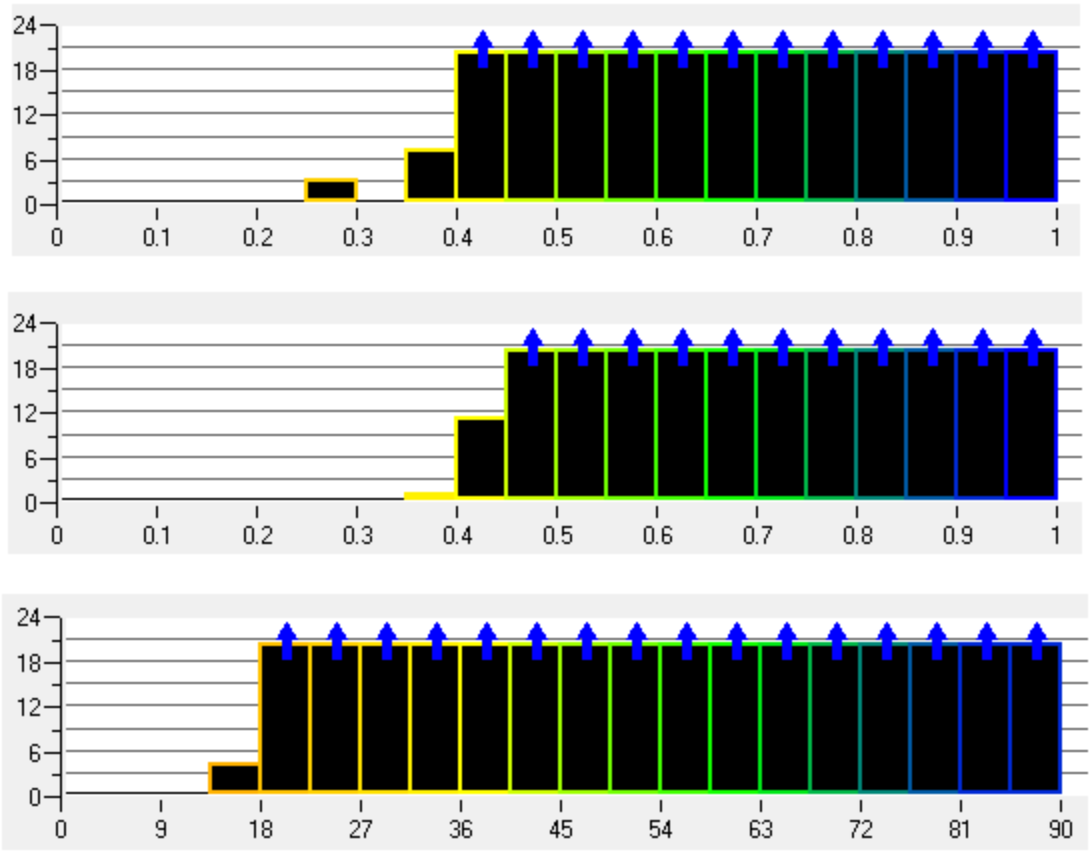

Figure 20: Histograms showing the quality, determinant 3x3x3, and minimum angle respectively for the Y junction mesh.

4.2.2 Y Junction Boundary and Operating Conditions

Two Y junction simulations were conducted. The air flowrate was varied between the two simulations. The first simulation used an air flowrate of 150 (l/min) which was used previously by both Brasil and Ahmed [6, 13]. The second simulation has a flowrate of 300 (l/min) which was previously used by Nguyen [14]. The change in flowrate of the air is the only difference between the two simulations and represents two different scavenge ratios of the sump. The water flowrate for both simulations is 75 (l/min). According to Figure 10, this puts both flows firmly in the slug flow region of the map. In both simulations, the outlet is set a pressure outlet at 0 Pa.

Similarly, to the bearing chamber simulations, both simulations were initialized with air only at both inlets. They were both run at steady state until the solution converged. Water was the added at the water inlet, and the simulation was run transiently.

For both Y Junction simulations, the following operating conditions are used:

1. Air density is 1.2 kg/m^3
2. Air dynamic viscosity is 1.7894 e-5 kg/m-s
3. Water density is 998 kg/m^3
4. Water dynamic viscosity is 1.003 e-3 kg/m-s
5. Gravity is -9.81 m/s^2
6. Surface tension between the air and oil is 0.072 N/m
7. Operating pressure is 101.325 kPa

4.2.3 Y Junction Models and Methods

Both Y junction simulations are modeled using the VOF model for two phase flow. Additionally, the SST k-ω model is used for turbulence simulation. A damping factor of 80 is applied to the turbulence model. Curvature correction is also applied to the turbulence model.

The SIMPLE method is used to solve the pressure-velocity coupling. A second order upwind discretization technique is used for the momentum, turbulent kinetic energy, and specific dissipation rate. The volume fraction is solved using a compressive technique. Lastly, the time step is solved using a first order implicit scheme. All residuals were said to have converged at a value of 1e-6.

A variable time step is used with a minimum time step of 1e-9 s and a maximum time step of 1e-3 s. The time step is determined so the CFL is .3. The maximum factor of change in the time step is set to 5 and the minimum factor of change is 0.5. The simulation ran until a transient time of 0.63 s was achieved.

4.2.4 Y Junction Results

The results for the first case with an air flowrate of 150 (l/min) and a water flowrate of 75 (l/min) can be seen in Figure 21. This simulation completed running in 51,500 time steps. This is 37,500 time steps less than Ahmed's T junction which needed 89,000 time steps to complete [6]. Figure 21 shows the water in red and the air in blue entering the system on the right at the two circles. The two phase flow then moves left and eventually flows through the outlet on the left. Figure 21 is a cross-sectional view of the outlet pipe, and each image advances in time as you progress down the figure. Figure 21 shows that at approximately 0.59 s, the air and water start to mix. Initially, the water appears to block the outlet pipe after the mixing point. However, the air then begins to form a bubble in the water flow. This bubble grows with time and at approximately 0.604 s separates the water into distinct regions. At this time, the water can be seen block the flow at the front of the pipe. This in the then proceeded by an air bubble. As the time increases, the water plugging

the flow begins to breakup. However, at the same time, a new plug begins to form near the mixing point. This is identical to what was seen in Ahmed's simulations [6].

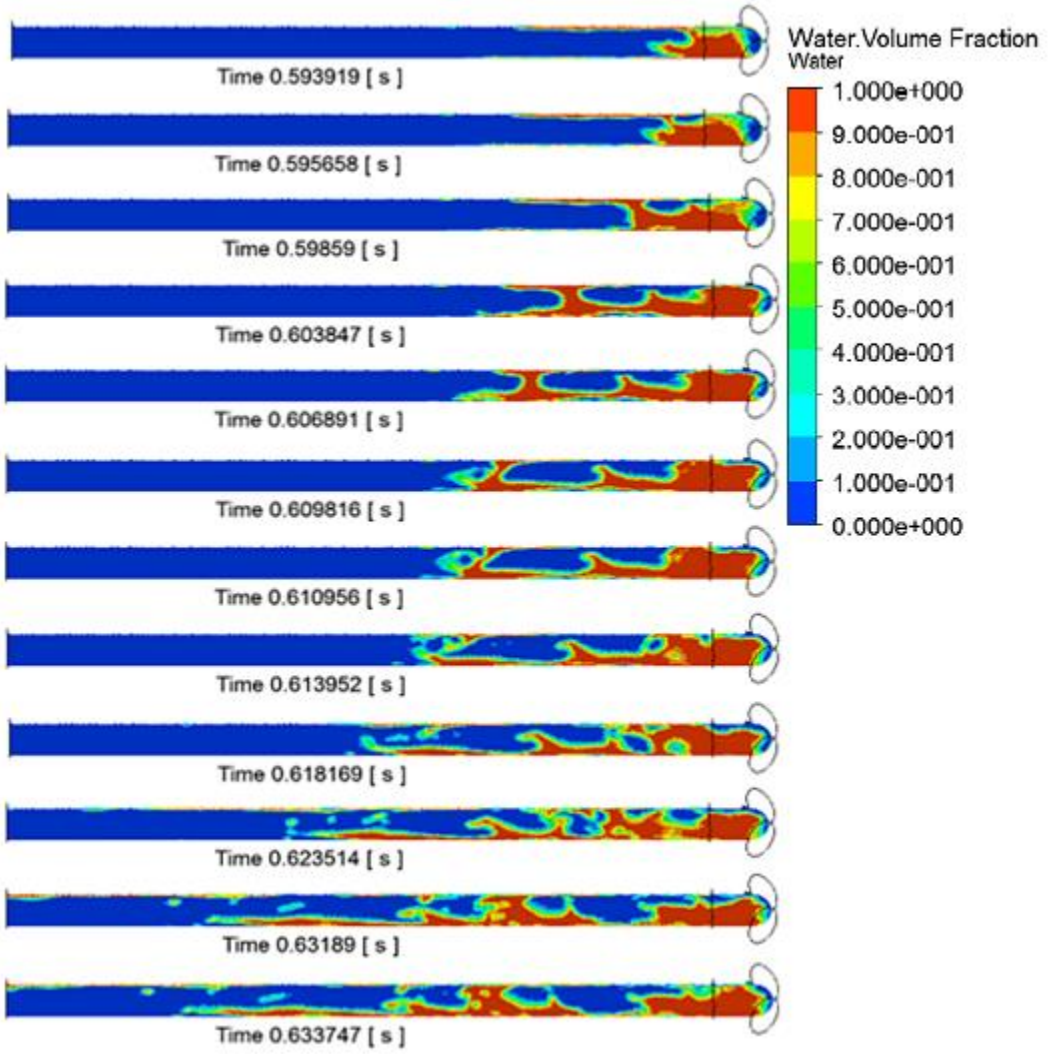

Figure 21: Cross-sectional view of the outlet pipe showing the water (75 l/min)) and air (150 l/min) creating slug flow.

Figure 21 shows the characteristic signs of slug flow. There is an initial section of water plugging the pipe followed by a bubble of air which in turn leads to another plug of water. While the first water plug does break up as the second plug is forming, slug flow was still achieved. In order to prevent the breakup of the plug in simulations, it is recommended that the length of the outlet pipe be reduced from 17.5 D1 to 7.5 D1. This allows the fluids to achieve slug flow while also preventing the breakup of the water plug.

Slug flow was achieved using a Y junction for a water flowrate of 75 (l/min) and an air flowrate of 150 (l/min). The Y junction required fewer time steps than Ahmed's T junction. Therefore it is recommended that the Y junction be used to accurately model the flow into the de-aerator but only with a shortened outlet pipe to prevent the breakup of the water plug.

Figure 22 shows the second Y junction case with a water flowrate of 75 (l/min) and an air flowrate of 300 (l/min). This case was completed in 66,000 time steps. Similar to Figure 21, the water in red and air in blue, enter the system on the right at the two circles. The water and air then flow to the left to the outlet. Similar to the 150 (l/min) case, the water initially plugs the outlet at 0.59 s. The air bubble then begins to grow and breaks off a section of water. Due to the increase in air flow between the two cases, the air bubble is significantly larger than in the 150 (l/min) case. Additionally, the water does plug the entire outlet pipe as in Figure 21. The air flows underneath the water plug. As the initial water plug begins to break up, a second plug forms similar to Figure 21. However, this plug is significantly smaller than the plug in Figure 21 and breaks up relatively early.

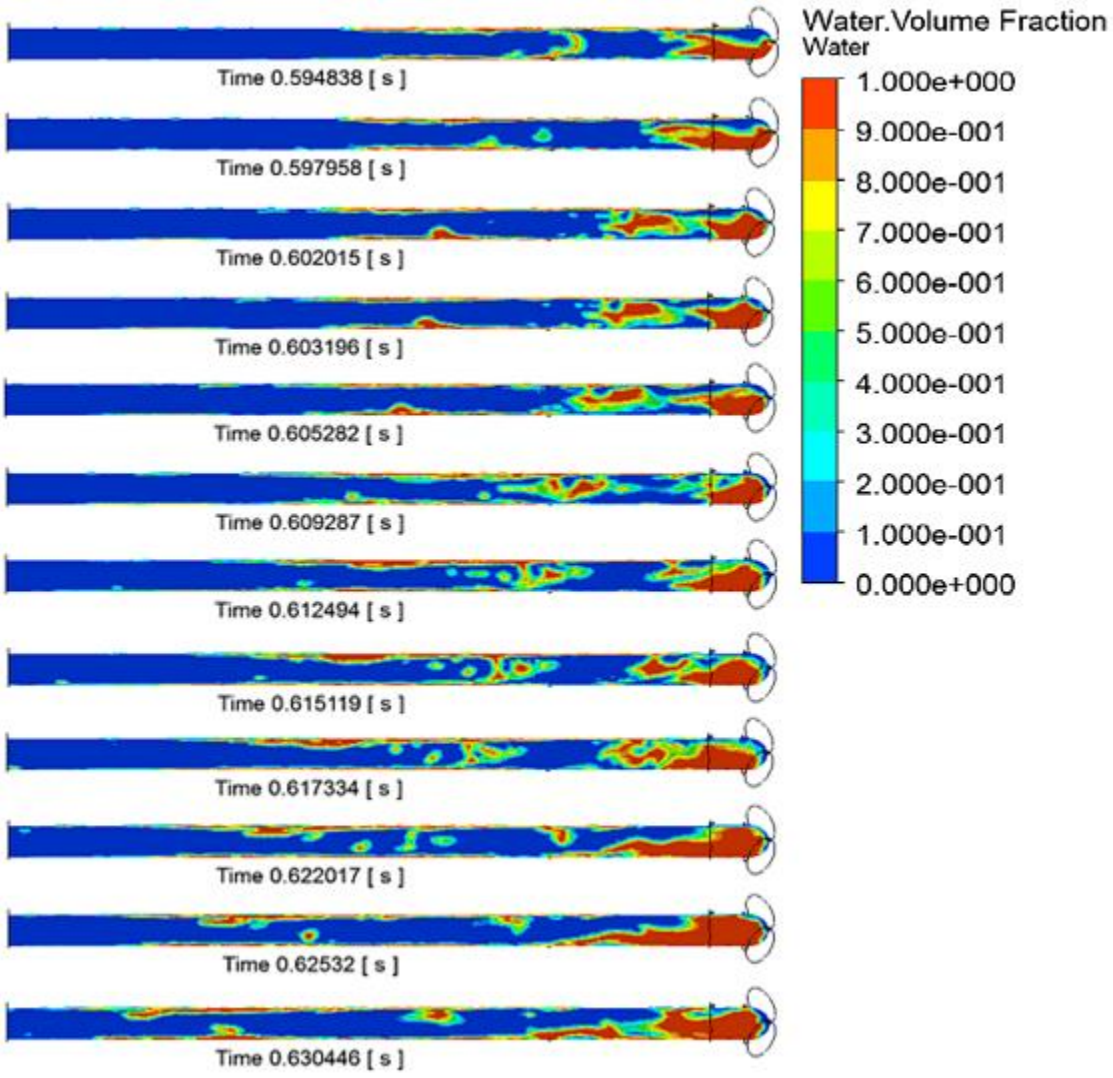

Figure 22: Cross-sectional view of the outlet pipe showing the water (75 l/min)) and air (150 l/min) creating slug flow.

The Y junction case of an air flowrate of 300 (l/min) and a water flowrate of 75 (l/min) driven almost entirely by the air flow. The water plugs are present but break up

quickly. Additionally, there appears to be little to no annular water flow underneath the air bubble. Therefore this would be classified as a slug/annular flow.

Figure 22 shows characteristics of slug flow; however, it is not pure slug flow. Ahmed did not conduct a simulation at flowrates of 300 (l/min) and 75 (l/min) for air and water respectively. Therefore, it is recommended that the Y junction be used for this case as well as it achieved the characteristic water plug for slug flow. Additionally, the Y junction simulations require fewer time steps than the T junction simulations. Similar to the previous case, it is recommended that the outlet pipe be shortened. However, the pipe should be shortened more than the previous case as the water plugs break up earlier in the 300 (l/min) air case. The outlet pipe should be shortened from 17.5 D1 to 6 D1 to prevent the breakup of the water plugs.

4.2.5 Y Junction Conclusion

In conclusion to the Y junction tests it recommended that a Y junction be used to accurately model the slug flow at the inlet of the de-aerator. The Y- junction achieved slug flow in both cases. However, in the 300 (l/min) air flowrate case, the flow appeared to be a cross of slug flow and annular flow. This is in contrast to the 150 (l/min) air flowrate case in which the flow showed more characteristics of slug flow. For the 150 (l/min) air flowrate case, the water formed complete plugs followed by an air bubble. However, for the 300 (l/min) air flowrate case, the water plugs were smaller and did not completely block the outlet pipe. Additionally, the air bubbles completely blocked the pipe and had no annular water flow underneath them.

For both cases, the first water plug began to break up at during the formation of the second water plug. In order to allow the water plugs to reach the outlet, it is recommended that the outlet pipe be shortened for both cases. For the 150 (l/min) air flowrate case, it is recommended that the outlet pipe be shortened from 17.5 D1 to 7.5 D1. For the 300 (l/min) air flowrate case it is recommended that the outlet pipe be shortened from 17.5 D1 to 6 D1.

Lastly, the Y junction case was able to run in significantly fewer time steps than Ahmed's T junction case. The Y junction case ran in 51,500 time steps for the 150 (l/min) air flow rate case and 66,000 time steps for the 300 (l/min) case. These are both shorter than Ahmed's T junction case which ran in 89,000 time steps [6]. Therefore, it is recommended that a Y junction with a shortened outlet pipe be used to model slug flow into the de-aerator for both the 150 (l/min) and 300 (l/min) air flowrate cases.

4.3 De-aerator

As previously stated the de-aerator is a part of the oil system within a jet engine. The function of the de-aerator is to separate the oil from the air so that the oil can be recycled into the bearing chambers to lubricate the turbine shaft. A pedestal has been placed within the de-aerator to allow oil to flow in between the pedestal and the de-aerator wall. The pedestal should block the air from flowing through the gap but prevent the oil from pooling on the pedestal surface. This research studies the effect of a conical pedestal of 30° with a 10.7% gap on the oil and air separation within the de-aerator.

Previous de-aerator research has been conducted experimentally by Brasil et al. and Nguyen et al. has shown that larger pedestal gaps create a better water efficiency for the system [13, 14]. However, these experimental results do not take into account the amount of air which escapes through the water outlet. Additionally, Nguyen tests show that the conical pedestal produces better water efficiency overall than the flat pedestal. However, as the pedestal gap increases, the effect of the conical pedestal becomes less significant.

The de-aerator has been studied using CFD by Ahmed and Morvan et al. [6, 11]. Morvan et al. concluded that a greater height to the de-aerator was beneficial as it provided more surface for the oil to separate over [11]. Ahmed conducted CFD research on a flat pedestal design and recommended a pedestal gap of 14.2% [6].

4.3.1 De-aerator Geometry and Mesh

The design of the de-aerator can be seen in Figure 23. This design shows the conical pedestal of this de-aerator. The dimensions for the de-aerator can be seen in Figure 24. In order to simplify the design, changes have been made from Ahmed's work [6]. These changes include replacing the long circular inlet pipe with a projected square surface inlet. This surface inlet is a square that has been projected onto the wall of the de-aerator. The square is then divided into two sections, a water inlet and a water and air inlet. The water inlet in blue is constantly inputting water into the de-aerator. The water and air inlet in green alternates between water and air based on a User Defined Function (UDF) which will be discussed further in the report. By alternating the air and water, slug flow can be achieved in the inlet. A square inlet was chosen because it significantly reduces the complexity of the mesh.

Furthermore, the two outlets located at the base of the de-aerator in Ahmed's design have been removed. These outlets have been replaced with one singular outlet at the base of the de-aerator. This also simplifies the meshing process and reduces the overall number of cells in the mesh.

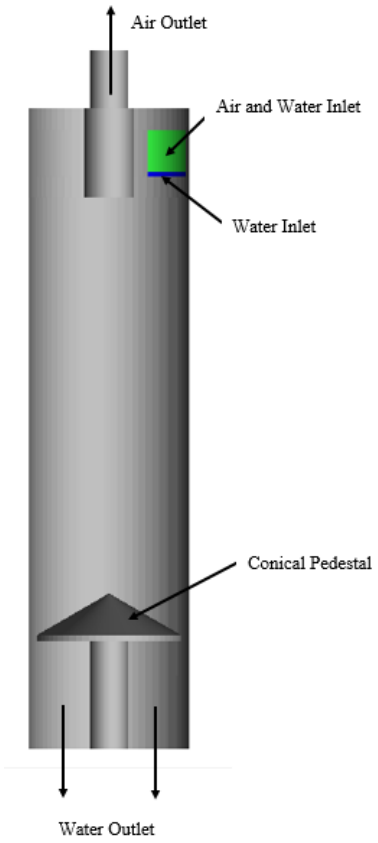

Figure 23: The de-aerator design, shows the conical pedestal as well as all inlets and outlets.

Figure 24 shows the dimensions of the de-aerator. As stated previously, all dimensions are in reference to the overall diameter of the de-aerator D2. The actual dimensions cannot be stated due to NDA restrictions. Not shown in Figure 24 is the angle of the de-aeartor pedestal is 30°. Additionally, the pedestal gap is 10.7% of the radius of the de-aerator.

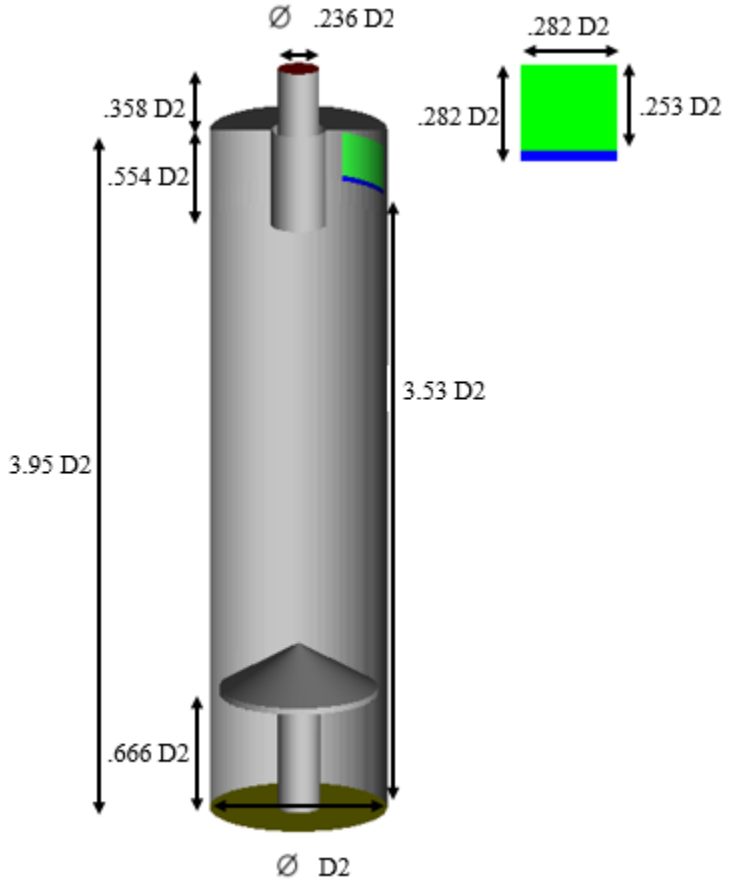

Figure 24: The de-aerator dimensions in terms of the overall de-aerator diameter.

Figure 25, Figure 26, Figure 27, Figure 28, and Figure 29 show the de-aerator surface meshes as well as the cross-sectional meshes. These figures show that the mesh is a hexahedral mesh. This is only possible with the square inlets. Having hexahedral mesh not only reduces the mesh size but also reduces the computation time for the simulation.

These figures show that the mesh refines in the areas near walls. The refinement is shown in black. This allows for the mesh to better compute the boundary layer at these regions. Additionally, all cells have a maximum 1.2 ratio of cell height growth between the cells. The 1.2 ratio value prevents errors caused from large changes in cells size [5].

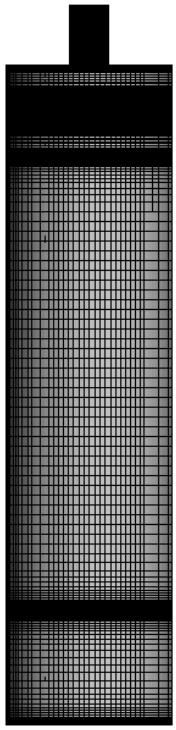

Figure 25: The surface mesh of the de-aerator. The black regions are areas of mesh refinement.

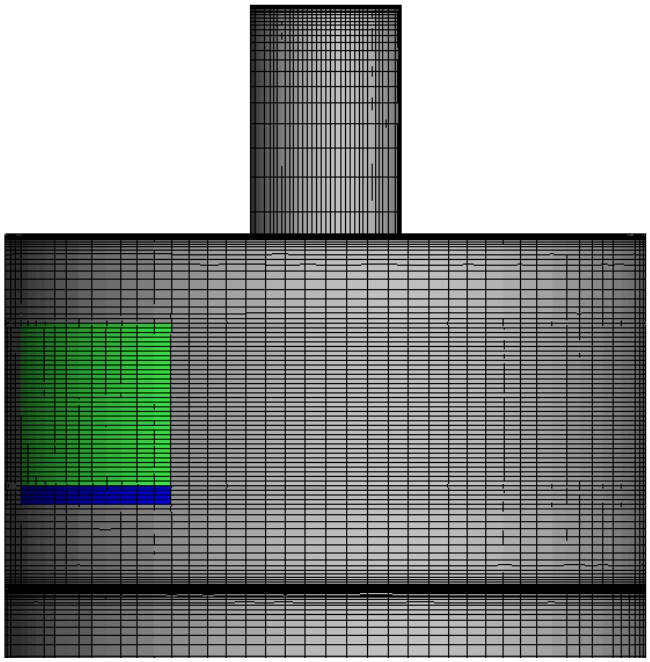

Figure 26: The top of the de-aerator surface mesh. It shows the projected water inlet in blue and the projected air and water inlet in green.

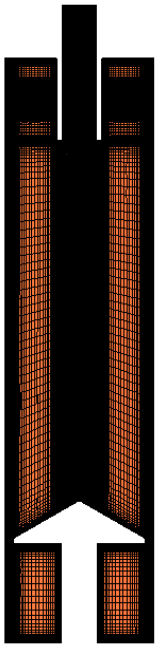

Figure 27: A cross-sectional view of the hexahedral mesh of the de-aerator. The regions of black show areas of mesh refinement.

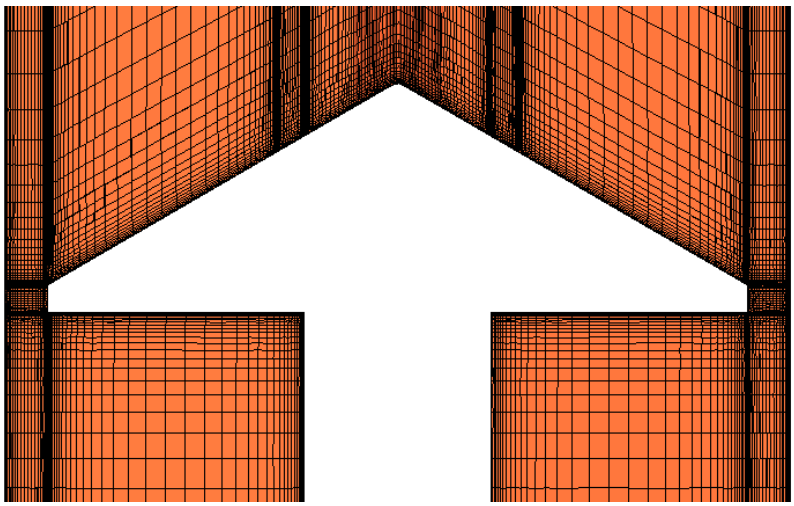

Figure 28: A cross-sectional view of the de-aerator mesh showing the refinement at the conical pedestal.

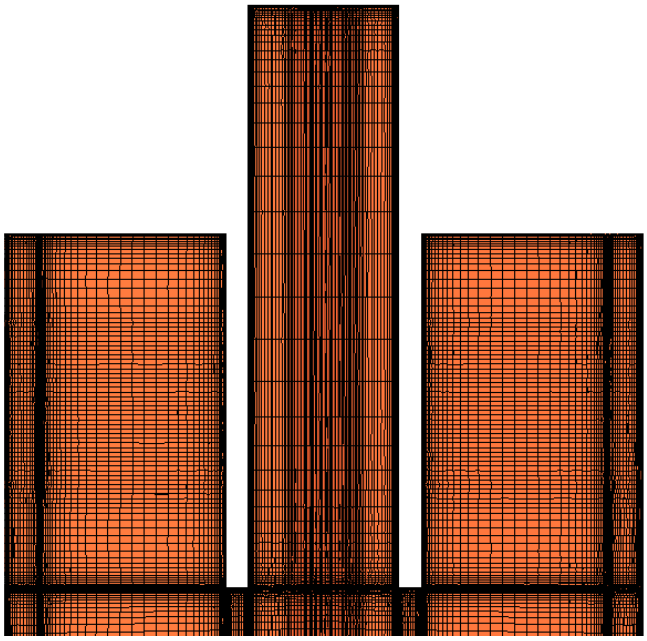

Figure 29: A cross-sectional view of the top of the de-aerator showing the mesh refinement.

Figure 30 shows the histograms depicting the mesh quality. The figure shows the quality, determinant 3x3x3, and the minimum angle respectively. For Fluent it is recommended that the quality and determinant 3x3x3 not be below 0.2. As shown in Figure 30, no cells are below this value for the quality or determinant 3x3x3. Additionally, it is recommended for Fluent that the minimum angle not be below 14° [28]. Figure 30 shows no cells are below 14°.

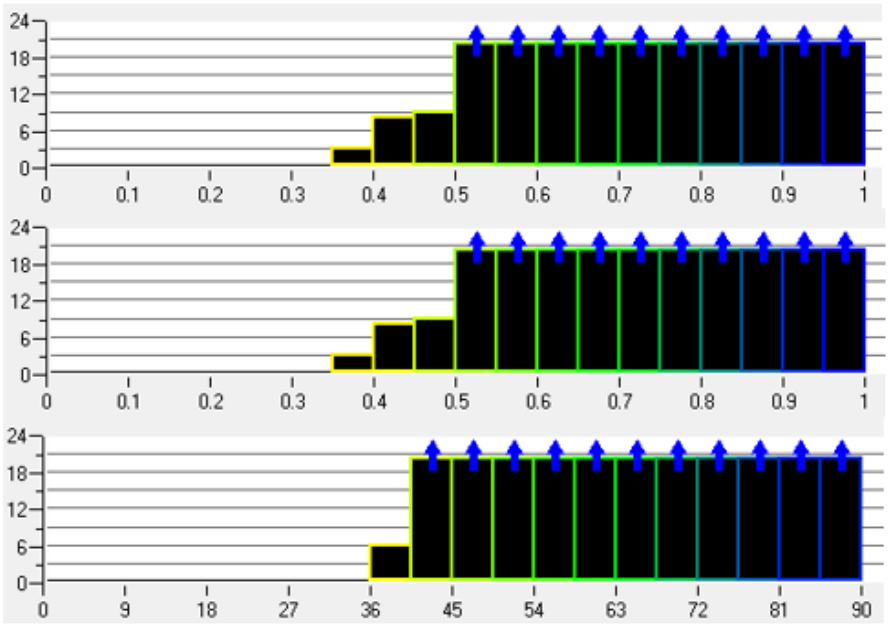

Figure 30: Histograms showing the quality, determinant 3x3x3, and min angle respectively of the de-aerator mesh.

4.3.2 De-aerator Boundary and Operating Conditions

The de-aerator simulation is set up so that both the water inlet and the air and water inlet operate at the same velocity. This simulation assumes a volumetric flowrate of 150 (l/min) of air and 75 (l/min) of water. In order to achieve slug flow in the inlet, a UDF was written which varies the flow at the air and water inlet between water and air. The UDF can be seen in Appendix A.

As shown in Figure 31, the UDF causes the water to act as a square function. The water is on for 0.0046 s at the air and water inlet and then off for 0.0142 s. The overall length of one period is 0.01881 s. This value was obtained from the high speed camera results obtained by Nguyen et al. [14]. All other values were used to maintain the appropriate flowrates of 75 and 150 (l/min) of water and air respectively. Additionally, as shown in Figure 31, the water is constantly on at the water inlet. While this UDF will create slug flow, the flow will not be as accurate as that created by the Y junction.

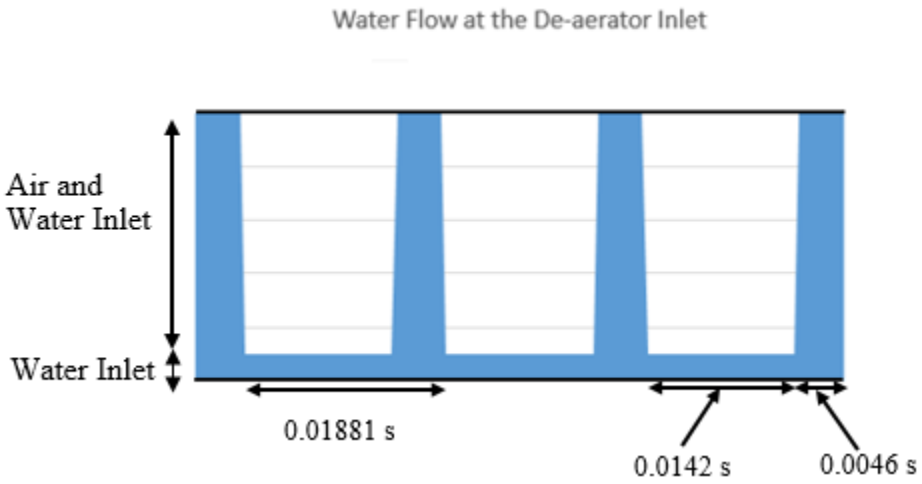

Figure 31: The water flow at the de-aerator inlet used to achieve slug flow.

The air outlet located at the top of the de-aerator and the water outlet located at the bottom of the de-aerator are set as pressure outlets with a gauge pressure of 0 Pa. This simulation was initialized using air only at steady state. Once the steady state simulation converged, the simulation was converted to transient two phase flow with water.

For the de-aerator simulation, the following operating conditions are used:

1. Air density is 1.2 kg/m^3
2. Air dynamic viscosity is 1.7894 e-5 kg/m-s
3. Water density is 998 kg/m^3
4. Water dynamic viscosity is 1.003 e-3 kg/m-s
5. Gravity is -9.81 m/s^2
6. Surface tension between the air and oil is 0.072 N/m
7. Operating pressure is 101.325 kPa

4.3.3 De-aerator Models and Methods

The de-aerator simulation is modeled using the VOF model for two phase flow. Additionally, the SST k-ω model is used for turbulence simulation. A damping factor of 80 is applied to the turbulence model. Curvature correction is also applied to the turbulence model.

The SIMPLE method is used to solve the pressure-velocity coupling. A second order upwind discretization technique is used for the momentum, turbulent kinetic energy, and specific dissipation rate. The volume fraction is solved using a compressive technique. Lastly, the time step is solved using a first order implicit scheme. All residuals were said to have converged at a value of 1e-6.

A variable time step is used with a minimum time step of 1e-9 s and a maximum time step of 1e-3 s. The time step will be determined so the CFL is .3. The maximum factor of change in the time step is set to 5 and the minimum factor of change is 0.5. The simulation was set to run until a transient time of 0.5 s was achieved.

4.3.4 De-aerator Results

The de-aerator simulation ran until a total time of 0.265 s. To reach 0.265 s a total of 222,500 time steps were needed. The simulation ran for approximately four weeks. Due to time constraints, the simulation was stopped and the data analyzed.

While the simulation did not run to completion, useful data can still be gained from the simulation. As shown in Figure 32, the UDF was successfully able to achieve slug flow. The figure shows the water volume fraction at the XY plane in the center of the de-aerator over time. The square to the left of each image represents the inlets. Initially, water can only be seen coming from the water inlet. However, at approximately 0.247 s, water can be seen from the left side of the air and water inlet. Gradually the whole air and water inlet fills with water. Then the water disappears from the left side and is gone at 0.252 s. The shift in water from left to right is due to the curvature of the air and water inlet. The left side of the air and water inlet is closer to the XY plane than the right side and therefore reaches the XY plane before the right side of the inlet.

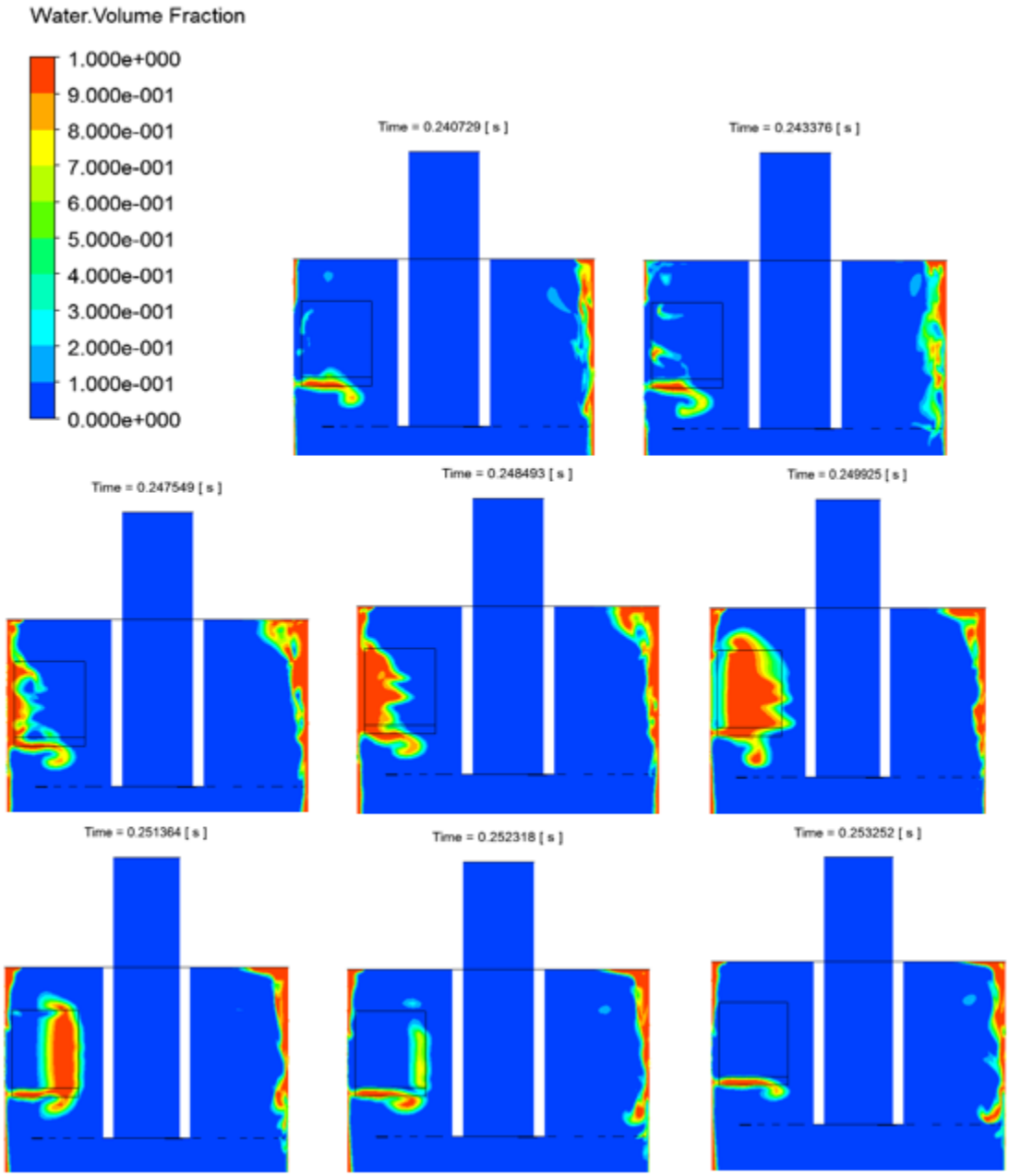

Figure 32: A diagram showing the slug flow progression from the inlet of the de-aerator.

In addition to successfully creating slug flow, water thickness data can be retrieved from the simulation. Figure 31 shows that there is little to no pooling on top of the de-aerator pedestal. The only pooling which occurs is at the top of the figure approximately 90° from the X axis. This is contrast to Ahmed's results which showed large amounts pooling on the top of the flat pedestal. Because of this reduction in pooling, I would recommend that the conical pedestal be used over the flat pedestal.

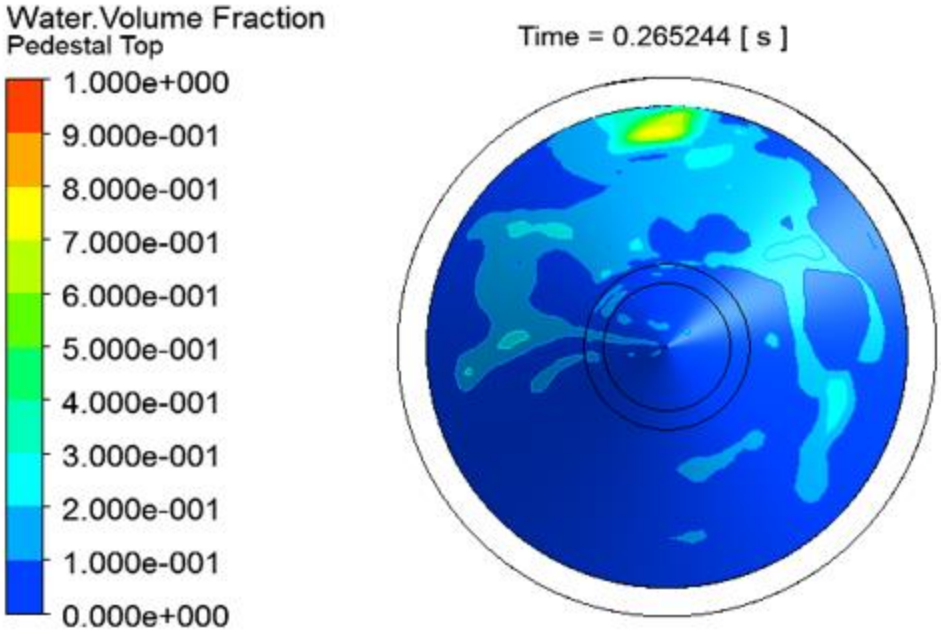

Figure 33: Water pooling on top of the de-aerator pedestal is little to none.

Figure 34 shows the water thickness in the pedestal gap at time of 0.236 s, 0.249 s and 0.265 s. Figure 34 shows that the water thickness is significantly less than the 10.7% pedestal gap. Graphs of the water thickness with respect to circumferential position around the de-aerator can be seen in Figure 35. These figures show that the water thickness reaches its maximum value at approximately 95°. The minimum water thickness is located at approximately 105° and appears to immediately follow the maximum water thickness. This is mostly likely the results of slug flow of the water creating a bump in the water thickness. The water thickness appears to be constant throughout the remainder of the pedestal gap.

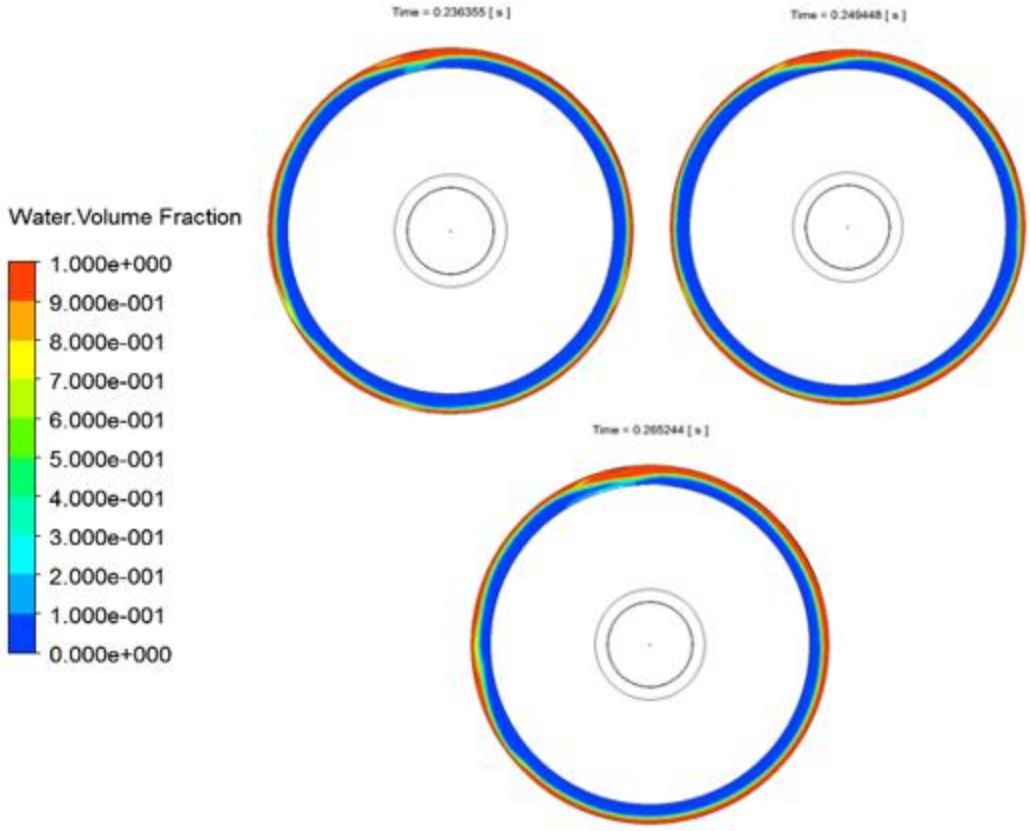

Figure 34: The de-aerator film thickness at 0.2363 s, 0.2494 s and 0.2652 s respectively.

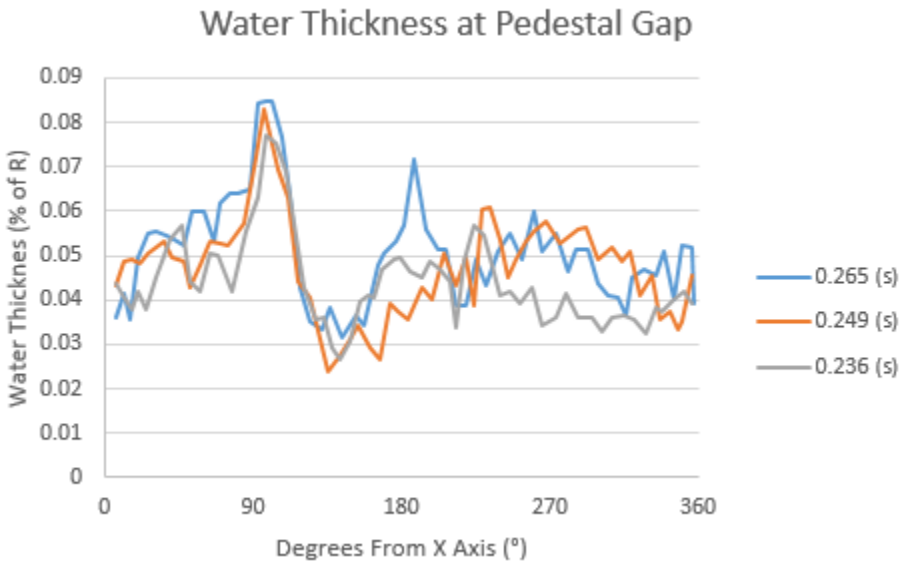

Figure 35: Water thickness in the pedestal gap at times of 0.265, 0.249, and 0.236 s.

Table 1: The Average and Maximum Water Thickness in the Pedestal Gap at 0.236, 0.249, and 0.265 s

Time (s)	Avg Water Thickness (% of R)	Max Water Thickness (% of R)
0.236	5.11	8.50
0.249	4.73	8.30
0.265	4.39	7.69

Table 1 shows that average water thickness and the maximum water thickness appear to increase with time. While this could be a result of the slug flow, this increase is mostly likely the results of the simulation not yet reaching a steady state. Therefore, it can be assumed that if the simulation progresses further, the water thickness will increase. The maximum water thickness at any time step is 8.5%. Additionally, in Nguyen's et al. research, she concluded that the water efficiency does not greatly improve between 8.3% and 9.5% [14]. Therefore, I would recommend further testing into conical pedestal at gaps between 8.3% and 9.5%.

4.3.5 De-aerator Conclusion

In conclusion, it was shown that the VOF method with a SST k-ω turbulence model could successfully simulate the flow within a de-aerator. For this simulation, a de-aerator with a pedestal gap of 10.7% was used as this provided the best water efficiency from experimental research. Additionally, slug flow was input into the de-aerator inlet using a UDF. The flowrates for the air and water were 75 and 150 (l/min) respectively.

Figure 32 showed that the UDF to create slug flow at the inlet was successful. However, this flow is not as accurate as the Y junction flows. Additionally, due to the curvature of the inlet, the front of the water plug curved as opposed to being flat. It can be seen in Figure 33 that pooling on top of the de-aerator pedestal was minimal compared to Ahmed's. This is due to the slant on the pedestal forcing the water into the pedestal gap. The water thickness within the pedestal gap was measured at varying time points. It shows that the maximum water thickness is in the same position, approximately 95°, for all times. This is a result of the slug flow creating a bump in the water thickness.

Lastly, it was shown that the average water thickness in the pedestal gap increased over time. This is mostly likely a result of the simulation not yet coming to a steady state. Due to time constraints, the simulation could not be run further. At the last time step of 0.265 s, the average water thickness was 5.11% and the maximum water thickness was 8.50%. Using this, as well as the experimental data taken from Nguyen et al., it is recommended that further investigation be conducted into pedestal gaps between 8.50% and 9.5% [14].

References

1. Han, J.-C., S. Dutta, and S. Ekkad, *Gas turbine heat transfer and cooling technology*. 2012: CRC Press.
2. Krug, M.B., et al., *Evaluation of Volume of Fluid Method for Numerical Modelling of an Aero Engine Bearing Chamber*, in *The 22nd International Symposium on Air Breathing Engines*. 2015: Phoenix, Arizona.
3. *The Jet Engine*, T.R.R. plc., Editor. 1986.
4. Boyce, M.P., *Gas turbine engineering handbook*. 2011: Elsevier.
5. Adeniyi, A.A., *A coupled Lagrangian-Eulerian framework to model droplet to film interaction with heat transfer*. 2015, University of Nottingham.
6. Ahmed, D., *CFD Investigation of Two Phase Flow in an Aeroengine De-aerator*, in *Mechanical, Material, and Manufacturing Engineering*. 2014, University of Nottingham: Rolls Royce University Technology Centre (UTC) in Gas Turbine Transmission Systems.
7. Carvalho, T.P., *A CFD study of the Trent-1000 breather sump area using VOF*, in *Mechanical Engineering*. 2012, University of Nottingham: Rolls-Royce University Technology Centre (UTC) in Gas Turbine Transmission Systems.
8. Adeniyi, A.A., H.P. Morvan, and K.A. Simmons. *A multiphase computational study of oil-air flow within the bearing sector of aeroengines*. in *ASME Turbo Expo 2015: Turbine Technical Conference and Exposition*. 2015. American Society of Mechanical Engineers.
9. Gorse, P., S. Busam, and K. Dullenkopf, *Influence of operating condition and geometry on the oil film thickness in aeroengine bearing chambers.* Journal of Engineering for Gas Turbines and Power, 2006. **128**(1): p. 103-110.
10. Chandra, B. and K. Simmons. *Transient two-phase effects in an aeroengine bearing chamber scavenge test rig*. in *ASME 2014 International Mechanical Engineering Congress and Exposition*. 2014. American Society of Mechanical Engineers.
11. H.P. Morvan, P.V., P. Rees, *Trent XWB De-aerator*. 2012, University of Nottingham: Rolls Royce University Technology Centre in Gas Turbine Transmission Systems.
12. Utikar, R., et al., *Hydrodynamic simulation of cyclone separators.* Computational fluid dynamics. Croatia: InTech, 2010.
13. Gustavo M Brasil, H.M., Paul Ress, *Investigation into the Effects of the Variation of the Inlet Geometry of a Cyclonic Air/Water Separator*. 2014, University of Nottingham: Rolls-Royce University Technology Centre (UTC) in Gas Turbine Transmission Systems.
14. Vy, N., et al., *Previous Works Study and Project Proposal for Aero-engine Deaerator Study*. 2015, University of Nottingaham: Rolls-Royce University Technology Centre (UTC) in Gas Turbine Transmission Systems.
15. Mokhatab, S. and W.A. Poe, *Handbook of natural gas transmission and processing*. 2012: Gulf Professional Publishing.
16. Azzopardi, B.J., *Gas-liquid flows*. 2006: Begell house New York.
17. Fan, Z., F. Lusseyran, and T. Hanratty, *Initiation of slugs in horizontal gas-liquid flows*. AIChE Journal, 1993. **39**(11): p. 1741-1753.

18. Taitel, Y. and A. Dukler, *A model for predicting flow regime transitions in horizontal and near horizontal gas-liquid flow.* AIChE Journal, 1976. **22**(1): p. 47-55.
19. Mandhane, J., G. Gregory, and K. Aziz, *A flow pattern map for gas—liquid flow in horizontal pipes.* International Journal of Multiphase Flow, 1974. **1**(4): p. 537-553.
20. Weisman, J., et al., *Effects of fluid properties and pipe diameter on two-phase flow patterns in horizontal lines.* International Journal of Multiphase Flow, 1979. **5**(6): p. 437-462.
21. Anderson, J., *Computational Fluid Dynamics*. 1995: McGraw-Hill Education.
22. Milne, W.E., *The numerical solution of differential equations*. 2d rev. and enl. ed. 1970, New York,: Dover Publications. xi, 359 p.
23. Courant, R., K. Friedrichs, and H. Lewy, *On the partial difference equations of mathematical physics.* IBM journal of Research and Development, 1967. **11**(2): p. 215-234.
24. Wilcox, D.C., *Turbulence modeling for CFD.* Vol. 2. 1998: DCW industries La Canada, CA.
25. Saad, T., *Turbulence modeling for beginners.* University of Tennessee space institute, 2011.
26. Boussinesq, J., *Essai sur la théorie des eaux courantes*. 1877: Imprimerie nationale.
27. Menter, F.R., *Zonal two equation k-turbulence models for aerodynamic flows.* AIAA paper, 1993. **2906**: p. 1993.
28. Inc., A., *Ansys Fluent Users's Guide*, A. Inc., Editor. 2015.
29. Egorov, Y., et al., *Validation of CFD codes with PTS-relevant test cases.* 5th Euratom Framework Programme ECORA project, 2004.
30. Hirt, C.W. and B.D. Nichols, *Volume of fluid (VOF) method for the dynamics of free boundaries.* Journal of computational physics, 1981. **39**(1): p. 201-225.
31. Patankar, S., *Numerical heat transfer and fluid flow*. 1980: CRC Press.

Appendix A: The Slug Flow UDF

```
/* UDF for setting VF of Water in the inlet */
/* at t<0.004588 sec the target VF is 1 */
/* when 0.004588<t<0.014223 sec the target VF is 0 */
/* The target VF then alternates from 1 for 0.004558 s to 0 for 0.014223 s */
#include "udf.h"
DEFINE_PROFILE(inlet_VF, thread, position)
{
real t, v;
face_t f;

begin_f_loop(f,thread)
{
t = RP_Get_Real("flow-time");
{
if(t < ceil(t/0.018812)*0.0045882927+(ceil(t/0.018812)-1)*0.0142237073 )
{
v = 1;
}
else
{
v = 0;
}
}
F_PROFILE(f,thread,position) = v;
}
end_f_loop(f,thread)
}
```